Revision 2

The effects of ferromagnetism and interstitial hydrogen on the equation of states of hcp and dhcp FeH_x: Implications for the Earth's inner core age

Hitoshi Gomi [a,b,*], Yingwei Fei [a], Takashi Yoshino [b]

[a] Geophysical Laboratory, Carnegie Institution of Washington, Washington, District of Columbia 20015-1305, USA.

[b] Institute for Planetary Materials, Okayama University, Misasa, Tottori 682-0193, Japan.

* Corresponding author. *E-mail address*: hitoshi.gomi@okayama-u.ac.jp

ABSTRACT

Hydrogen has been considered as an important candidate of light elements in the Earth's core. Because iron hydrides are unquenchable, hydrogen content is usually estimated from in-situ X-ray diffraction measurements assuming the following linear relation: $x = (V_{FeHx} - V_{Fe}) / \Delta V_H$, where x is the hydrogen content, ΔV_H is the volume expansion caused by unit concentration of hydrogen, V_{FeHx} and V_{Fe} are volumes of FeH_x and pure iron, respectively. To verify the linear relationship, we computed the equation of states of hexagonal iron with interstitial hydrogen by using the Korringa-Kohn-Rostoker method with the coherent potential approximation (KKR-CPA). The results indicate a discontinuous volume change at the magnetic transition and almost no compositional (x) dependence in the ferromagnetic phase at 20 GPa, whereas the linearity is confirmed in the non-magnetic phase. In addition to their effects on density-composition relationship in the Fe-FeH_x system, which is important for estimating the hydrogen incorporation in planetary cores, the magnetism and interstitial hydrogen also affect the electrical resistivity of FeH_x. The thermal conductivity can be calculated from the electrical resistivity by using the Wiedemann-Franz law, which is a critical parameter for modeling the thermal evolution of the Earth. Assuming an $Fe_{1-y}Si_yH_x$ ternary outer core model ($0.0 \leq x \leq 0.7$), we calculated the thermal conductivity and the age of the inner core. The resultant thermal conductivity is ~100 W/m/K and the maximum inner core age ranges from 0.49 to 0.86 Gyr.

Keywords: FeH_x; ferromagnetism; chemical disorder; equation of states; KKR-CPA;

INTRODUCTION

Seismologically inferred density profile of the Earth interior suggests that some amounts of light alloying elements are incorporated into iron-based metallic core (Birch, 1964). Hydrogen is one of the important light element candidates in the Earth's core, because only a small amount of interstitial hydrogen may drastically change the physical properties of iron at high pressure, e.g. crystal and magnetic structure (e.g. Isaev et al., 2007; Elsässer et al. 1998; Pépin et al., 2014), melting temperature (e.g. Yagi and Hishinuma, 1995; Okuchi, 1998; Sakamaki et al., 2009; Shibazaki et al., 2011; 2014), density and elastic properties (Caracas, 2015; Hirao et al., 2004; Mao et al., 2004; Pépin et al., 2014; Shibazaki et al., 2012; Tagawa et al., 2016; Umemoto and Hirose, 2015). The maximum abundance of hydrogen has been estimated to be $0.3 \leq x \leq 0.5$ (in atomic ratio) for the Earth's core (Okuchi, 1997; Narygina et al., 2011; Umemoto and Hirose, 2015). Furthermore, recent experimental study on hcp Fe-Si-H ternary alloys suggests that the abundance of alloying hydrogen is $x = 0.17$ (Tagawa et al., 2016). These results rely on our knowledge of non-stoichiometric phases such as FeH_x.

Investigation of non-stoichiometric FeH_x is not an easy task for both experimental and theoretical studies. Experimental measurements on non-stoichiometric FeH_x alloys have been very limited (Yamakata et al., 1992; Antonov et al., 1998; Shibazaki et al., 2014; Machida et al., 2014; Tagawa et al., 2016; Iizuka-Oku et al., 2017), because most of the previous experiments on Fe-H system were conducted under hydrogen-saturated conditions. On the other hand, theoretical studies have the advantage of simulating non-stoichiometric FeH_x alloys by means of super-cell technique (e.g. Caracas, 2015; Umemoto and Hirose, 2015). However, such method requires large super cell to

57 calculate arbitrary concentration of hydrogen. Furthermore, the calculated results are
58 influenced by the geometry of the super cell (Caracas, 2015).

59 Here we report results of the total energy and the band structure of FeH_x alloys
60 obtained by means of first-principles calculations based on the Korringa-Kohn-Rostoker
61 method (KKR) (e.g. Akai, 1989). The coherent potential approximation (CPA) is
62 adopted to deal with the alloying effect, which is a complementary approach to the
63 super-cell method. In this study, we focused on the equation of state (EoS) of hexagonal
64 close-packed (hcp) and double hexagonal close-pack (dhcp) iron hydrogen alloys FeH_x,
65 in order to evaluate the effect of ferromagnetism and interstitial hydrogen. The results
66 demonstrate the non-linear volume change with hydrogen content due to magnetic
67 transition. We will discuss on the validity of estimation of hydrogen content by in situ
68 X-ray diffraction. Another pronounced feature of the CPA is the explicit representation
69 of broadening of band structure due to disorders, which is closely related to the
70 electrical resistivity (Gomi et al., 2016). Finally we will discuss the implications for
71 alloying hydrogen in the Earth's and planetary cores.

72 **METHODS**

73 We performed static first-principles calculations of hcp and dhcp iron-hydrogen
74 alloys. The Korringa-Kohn-Rostoker (KKR) method was used as implemented in the
75 AkaiKKR code (Akai, 1989). Perdew-Burke-Ernzerhof (PBE) type of generalized
76 gradient approximation (GGA) was used for the exchange-correlation functional
77 (Perdew et al., 1996). The relativistic effects are taken into account within the scalar
78 relativistic approximation. The wave functions are calculated up to $l = 2$, where l is the
79 angular momentum quantum number. The coherent potential approximation (CPA) was

used to represent hydrogen atoms, which randomly occupied the octahedral interstitial site. The hydrogen content x varied from 0.0 (pure iron) to 1.0 (hydrogen saturated iron hydrides) with 0.1 step. The axis ratio is optimized by the total energy minimum at each volume. The number of k-points is set to be at least 312 in the irreducible Brillouin zone. Both spin polarized and non-spin polarized calculations were carried out to represent ferromagnetic and non-magnetic states, respectively. The local moment disorder (LMD) state is also simulated, which is an analog of the paramagnetic state above the Curie temperature (Akai and Dederichs, 1993; see also supplementary text). The energy difference between ferromagnetic and LMD state indicates the relative stability of the ferromagnetism with regards to temperature. Applying the Heisenberg model, the energy difference gives rough value of the Curie temperature, T_c:

$$T_C = \frac{2}{3k_B}(E_{\mathrm{LMD}} - E_{\mathrm{ferro}}) \quad (1)$$

where k_B is the Boltzmann constant, E_{LMD} and E_{ferro} are total energies of LMD and ferromagnetic states, respectively. This method is used by computational material design of stable magnet for industrial purpose (Sato et al., 2003).

RESULTS

Fig. 1 shows the total energies of hcp and dhcp, non-magnetic and ferromagnetic FeH_x alloys as a function of volume. In general, non-magnetic phases have smaller V_0 than those of ferromagnetic phases. For pure Fe, the most stable phase is non-magnetic hcp Fe with equilibrium volume per formula unit (f.u.) of V_0 = 70.58 $Bohr^3$/f.u. (10.46 $Å^3$/f.u), followed by ferromagnetic dhcp, non-magnetic dhcp and ferromagnetic hcp Fe at zero pressure. For $FeH_{1.0}$, the relative stability is in order of ferromagnetic dhcp,

ferromagnetic hcp, non-magnetic dhcp and non-magnetic hcp. At higher pressure, relative phase stability can be obtained by comparison of the enthalpy, $H(V) = E(V) + PV$. In order to calculate the pressure, we used the 3rd-order isothermal Birch-Murnaghan equation of states (EoS). First, we fitted the total energy to the *E*-*V* relation:

$$E(V) = E_0 + \frac{K_0 V}{K'(K'-1)}\left[K'\left(1-\frac{V_0}{V}\right)+\left(\frac{V_0}{V}\right)^{K'}-1\right], \quad (2)$$

where E is the total energy, K and K' are the bulk modulus and its pressure derivative, and V is the volume. Subscript 0 indicates zero pressure value. Supplementary Tables S1-4 show the fitting parameters. Pressures were then calculated by using the *P*-*V* relation:

$$P(V) = \frac{3K_0}{2}\left[\left(\frac{V_0}{V}\right)^{\frac{7}{3}}-\left(\frac{V_0}{V}\right)^{\frac{5}{3}}\right]\left\{1+\frac{3}{4}(K'-4)\left[\left(\frac{V_0}{V}\right)^{\frac{2}{3}}-1\right]\right\}. \quad (3)$$

EoS of ferromagnetic and nonmagnetic dhcp $FeH_{1.0}$ and nonmagnetic hcp Fe are shown in Fig. 2a. Our calculated results of ferromagnetic dhcp $FeH_{1.0}$ are consistent with previous results obtained from diamond-anvil cell (DAC) experiments at low pressure (Hirao et al., 2004; Pépin et al., 2014). However, the calculated volume of ferromagnetic dhcp $FeH_{1.0}$ deviates at about 30 GPa, and the non-magnetic result approaches to the experimentally determined volumes at around 60 GPa. This behavior is consistent with previous calculations (e.g. Elsässer et al. 1998; Tsumuraya et al., 2012; Pépin et al., 2014). Similarly, our hcp Fe results broadly reproduce the compression curve of hcp Fe determined by DAC studies (Fei et al, 2016; Dewaele et al., 2006). Fig. 2b shows the Curie temperature of dhcp $FeH_{1.0}$, which is comparable to the Curie temperature of bcc iron at ambient pressure.

The same procedure was applied to non-stoichiometric FeH_x alloys calculated by using the CPA. With increasing hydrogen content, V_0 of each phase becomes larger, and hence, ferromagnetic phase tends to become stable (Fig. 1). On the contrary, the pressure effect favors smaller volume phases, which leads to the collapse of ferromagnetism at high pressure. Fig. 2c indicates the most stable crystal/magnetic structure among these four combinations as functions of pressure and hydrogen content. Within the stability field of the ferromagnetic dhcp, the Curie temperature is also shown by broken lines (Fig. 2c).

DISCUSSION

Magnetic transition pressure

One of the critical discrepancies between first-principles prediction and experimental observation is the magnetic transition pressure. Elsässer et al. (1998) predicted that the stable magnetic structure of FeH is the ferromagnetic, and it transforms to non-magnetic phase at about 60 GPa. This transition pressure is reproduced by subsequent first-principles studies (Pépin et al., 2014; Tsumuraya et al., 2012), further supported by this study (Fig. 2). However, previous DAC experiments implied much lower transition pressure. Mao et al. (2004) conducted nuclear resonant X-ray scattering (NRIXS) experiments up to 52 GPa to obtain compressional velocity and shear wave velocity of FeH. They found the change in slope of these velocity plots above 22 GPa. Shibazaki et al. (2012) performed inelastic X-ray scattering (IXS) measurements up to 70 GPa, and also found similar anomaly at around 30 GPa. Such an anomaly has been interpreted as the magnetic transition from ferromagnetic to non-magnetic state. Indeed, these transition pressures are much lower than theoretical predictions. The local magnetic

147 moments of two Fe sites in dhcp FeH_x have slightly different value, and they are
148 quenched almost simultaneously with compression, which is consistent with previous
149 calculation (Tsumuraya et al., 2012). In addition to the generalized gradient
150 approximation (GGA) for the exchange correlation functional, which likely
151 overestimates the stability field of large volume phases (i.e. ferromagnetic phase), we
152 consider the effect of finite temperature, based on the experimental fact that the Curie
153 transition is second-order phase transition. Previous X-ray diffraction (XRD)
154 measurements (Hirao et al., 2004; Pépin et al., 2014) suggest that the EoS of dhcp FeH
155 is consistent with first-principles EoS of its ferromagnetic phase at pressures below ~30
156 GPa, but the experimental results become gradually deviate from theoretical prediction
157 of ferromagnetic FeH. At pressures above 50 GPa, the experimental data become
158 consistent with theoretical EoS of non-magnetic FeH again. Mitsui and Hirao (2010)
159 conducted *in-situ* Mössbauer measurement up to ~65 GPa. They found rapid
160 disappearance of ferromagnetic 6-line pattern at 27.6 GPa, but there still remains
161 residual weak hyperfine field up to 64.7 GPa. In order to assess the stability of
162 ferromagnetism relative to the paramagnetic state with randomly distributed the
163 momentum directions, we calculated the total energy of the LMD state. The calculated
164 Curie temperature decreases rapidly with applying pressure, and becomes comparable to
165 the ambient temperature at the highest pressure. This behavior is consistent with
166 previous Mössbauer spectroscopy measurements reported by Mitsui and Hirao (2010),
167 as well as XRD study by Hirao et al. (2004). In this study, we only considered the
168 ground state ferromagnetism and the LMD state at the Curie temperature. The
169 contribution to the free energy of intermediate temperature magnetism, as well as finite
170 temperature phonon and fcc phase transition, need to be investigated in the future.

171 Furthermore, it is also important to investigate the sound-wave velocity around the
172 magnetic transition.

173 **Volume of FeH_x alloys**

174 Thermodynamic calculations suggest that the solubility of hydrogen is significantly
175 enhanced at high hydrogen pressure over 3.5 GPa, whereas hydrogen is hardly dissolved
176 into iron at ambient conditions (Sugimoto and Fukai, 1992; Fukai, 1992). This is
177 confirmed from *in-situ* XRD experiments, which show a large volume difference
178 between Fe and FeH_x caused by the occupation of hydrogen atoms into the interstitials
179 (e.g. Hirao et al., 2004; Narygina et al., 2011; Pépin et al., 2014). Against the difficulties
180 arising from the fact that high-pressure polynomials of iron-hydrides cannot be
181 quenched to ambient pressure and temperature, some experiments were conducted to
182 determine the hydrogen or deuterium content at high pressure. Okuchi (1997; 1998)
183 measured the volume fraction of hydrogen bubbles in the iron grains of a recovered
184 sample by means of a rapid-decompression technique. Antonov and co-workers
185 successfully quenched the FeH_x sample to ambient pressure and low temperature by
186 pre-cooling of the sample below 150 K before releasing the pressure, and conducted
187 outgassing (Schneider et al., 1991) and neutron diffraction measurements (Antonov et
188 al., 1998). Recently, Machida et al. (2014) and Iizuka-Oku et al. (2017) reported results
189 from *in-situ* neutron diffraction measurements. However, the maximum pressures of
190 these studies are limited to less than 10 GPa. At higher pressures, *in-situ* XRD
191 measurement is the most common way to determine the volume of FeH_x. In order to
192 estimate the hydrogen content from its volume, the following linear
193 volume-composition relationship is widely used,

194 $$x = \frac{V_{FeH_x} - V_{Fe}}{\Delta V_H} \quad (4)$$

195 where x is hydrogen content, V_{FeHx} is the volume of FeH_x per formula, V_{Fe} is the atomic
196 volume of iron, and ΔV_H is volume increase per hydrogen atom (see also supplementary
197 text). The ΔV_H has been assumed to be independent of x. This relationship is applicable
198 to several face-centered cubic (fcc) metal-hydrogen alloys, which is confirmed from
199 degassing methods (Fig. 3a) (see review in Fukai, 2006). To test the applicability of our
200 first-principles calculations, we first calculated the equilibrium volume of fcc
201 metal-hydrogen alloys (PdH_x, NiH_x, $Ni_{0.8}Fe_{0.2}H_x$ and $Fe_{0.65}Ni_{0.29}Mn_{0.06}H_x$). Our
202 first-principles results are broadly consistent with previous experimental results (Fukai,
203 2006), which show nearly linear volume expansion as a function of hydrogen content,
204 as predicted by Eq. (4) (Fig. 3a). Fig. 3b shows the volume of the most stable phase and
205 non-magnetic phase of FeH_x as a function of hydrogen content at 20 GPa. Fig 3c
206 presents the $\Delta V_H = (V_{FeHx} - V_{Fe})/x$. The figures clearly indicate the violation of linearity.
207 At $x < 0.4$, where the non-magnetic hcp FeH_x phase is stable, the volume increases
208 almost linearly. However, a discontinuous increase of volume occurs across the phase
209 transition from non-magnetic hcp to ferromagnetic dhcp phase. Within the
210 ferromagnetic phase, the volume is almost independent of hydrogen content, suggesting
211 that the volume of FeH_x phase is mostly controlled by ferromagnetism. Recently,
212 Iizuka-Oku et al. (2017) reported the result of *in-situ* neutron diffraction measurements
213 on fcc FeD_x. They compressed Fe with $Mg(OD)_2$ and SiO_2 mixture as a deuterium
214 source. The sample was heated to ~ 1000 K at ~ 4 GPa. During the 12 hours holding
215 time, the Fe sample was progressively deuterated, which is confirmed by the volume
216 increase and the 111/200 diffraction intensity ratio of fcc FeD_x. The volume expansion

exhibited non-linear behavior as a function of the holding time, which might partly be related to the magnetic transition.

The volume of ferromagnetic alloys has been interpreted in term of average magnetic moment (see Shiga, 1974 for Review). For example, the lattice constant of Fe-Co system has a maximum at the top of the Slater-Pauling curve. In case of the Fe-H system, the magnetic element is iron only. Therefore, the bulk magnetic moment is almost independent of hydrogen concentration. This is consistent with our first-principles prediction showing little dependence of x on the volume. The Eq. (4) is widely used by many previous studies to estimate the hydrogen content of iron hydride at high pressure (e.g. Yagi and Hishinuma, 1995; Shibazaki et al., 2011; Terasaki et al., 2012; Tagawa et al., 2016). However, our results suggest possible overestimates of the hydrogen content in these experiments because of the assumed linear relationship. Fig. 3b also shows that the volume of non-magnetic phase follows the linear relationship predicted by Eq. (4). Such linearity is also observed in non-magnetic phases at higher pressure. Therefore, the Eq. (4) can be applied at pressures higher than ~65 GPa.

Electrical resistivity

It is also worth to mention the effect of magnetism and interstitial hydrogen on the electrical resistivity, since the electrical resistivity, and relevant thermal conductivity, is crucial for the thermal evolution of the Earth (de Koker et al., 2012; Pozzo et al., 2012; Gomi and Hirose, 2015; Gomi et al., 2013; 2016; Seagle et al., 2013; Konôpková et al., 2016; Ohta et al., 2016; Suehiro et al., 2017). The total resistivity of Fe alloys at the core conditions involves many scattering mechanisms, namely phonon scattering, impurity scattering, magnetic scattering and electron-electron correlations. Among them, impurity resistivity of alloying elements is predicted to be predominant and the effect of

241 spin disordered resistivity has been neglected at the Earth's core (see Supplementary Fig.
242 S5 of Gomi et al., 2016). As shown in Gomi et al. (2016), the life time and the mean
243 free path of electrons are relevant to the degree of broadening of the band structure in
244 the vicinity of the Fermi energy via uncertainty relationship. Therefore, we can
245 qualitatively estimate the electrical resistivity from the band structure.

246 Fig. 4a shows the band structure of non-magnetic dhcp Fe. At the stoichiometric
247 composition, the band structure has no broadening because it has no disorder. The
248 broadening increases with increasing hydrogen content, and reaches a maximum at x =
249 0.5, which is the highest chemical disorder (Fig. 4c). Above x = 0.5, it decreases with
250 recovering the ordering (Fig. 4e). However, it is found that the broadening mainly
251 occurred at far below the Fermi level. This is consistent with the fact that the hydrogen *s*
252 states locate at around -0.6 Ry from the Fermi energy (Tsumuraya et al., 2012). Even if
253 we considered the electron temperature, the half width at half maximum of the
254 Fermi-Dirac distribution function is 5.58×10^{-2} Ry at T = 5000 K (see Supplemental
255 text for detail). Because only electrons at the vicinity of the Fermi energy can contribute
256 the electrical conduction, the effect of disordered hydrogen atoms is predicted to be
257 insignificant to the impurity resistivity.

258 On the other hand, the band structures of LMD state exhibit a strong broadening
259 around the Fermi energy (Fig. 4f-j), which is consistent with the fact that the spin
260 magnetic moment of Fe 4*d* electrons dominates the bulk magnetic moment of FeH_x. As
261 well as the impurity resistivity, this broadening contributes to the electrical resistivity as
262 the spin disordered resistivity (Glasbrenner et al., 2014; Ebert et al., 2015). Considering
263 that both the magnetic moment and the Curie temperature of ferromagnetic hcp and
264 dhcp FeH are comparable to those of bcc Fe, the spin disordered resistivity could be at

the same level with that of bcc Fe. This value is comparable to the saturation resistivity, and consistent with previous high *P*-*T* resistance measurement of dhcp FeH (Antonov et al., 2002).

Previous high pressure and room temperature resistance measurements on dhcp FeH_x showed similar pressure dependence with pure hcp Fe (Matsuoka et al., 2011, Gomi et al., 2013). Assuming that the composition is close to the stoichiometric composition (x = 1.0), dominant scattering mechanism may be lattice vibration. Therefore, the phonon-contributed resistivity of dhcp FeH_x may be comparable to that of hcp Fe.

In summary, we considered here three scattering mechanisms on FeH_x alloys at high pressure; impurity resistivity, spin disordered resistivity, and phonon-contributed resistivity. Impurity resistivity of interstitial hydrogen is predicted to be small, whereas that of substitutional silicon is predominant in hcp Fe-Si alloy (Gomi et al., 2013; 2016; Seagle et al., 2013). On the other hand, spin disordered resistivity may have significant contribution within the stable pressure-composition range of ferromagnetic phase at high temperature. Phonon-contributed resistivity of FeH_x may not be significantly different from pure Fe. Thus, we predict that the spin disordered resistivity is predominant at around the Curie temperature and below the magnetic transition pressure, and it will largely decrease in conjunction with the disappearance of its magnetism.

IMPLICATIONS

The calculations indicate that ferromagnetism in FeH_x collapses above ~65 GPa, accompanied with significant changes in physical properties. One of the important findings of this study is the absence of strong scattering mechanism in FeH_x alloys at the Earth's core conditions. Gomi et al. (2016) found that the Si impurity resistivity is

predominant in Fe-Ni-Si ternary alloy at the core *P-T* conditions (see Supplementary Fig. S5 of Gomi et al., 2016). However, we predict that H impurity should not contribute to the electron scattering (Fig. 4 a-e). Another possible scattering mechanism is magnetic disorder (Drchal et al., 2017). Although it indeed exhibits strong broadening of the band structure (Fig.4 f-j), the ferromagnetic state becomes unstable above ~ 60 GPa, leading to no contribution to resistivity of the Earth's core. Therefore, if hydrogen were the predominant alloying light elements in the Earth's core, the total core resistivity would be smaller than our previous estimates based on Fe-Ni-Si ternary core model (Gomi et al., 2016).

In order to understand the thermal evolution of hydrogen-bearing Earth's core, we develop an $Fe_{1-y}Si_yH_x$ ternary composition model for the Earth's outer core as follows. First, we modeled the outer core temperature as function of hydrogen content, x. The melting temperature of pure Fe at the inner core boundary (ICB) pressure is extrapolated to be ~6200 K (Anzellini et al., 2013; Alfè, 2009), and that of $FeH_{1.0}$ is ~3500 K (Sakamaki et al., 2009). Note that Si may not significantly decrease the melting temperature (Fischer et al., 2013). Assuming that the melting temperature reduction is proportional to x, the present-day ICB temperature may be $T_{\mathrm{ICB}p}(x) = 6200 - 2700x$ K. The CMB temperature can be estimated from the adiabatic temperature gradient, $T_{\mathrm{CMB}p}(x) = T_{\mathrm{ICB}p}(x)\left(\rho_{\mathrm{CMB}}^{densiy} / \rho_{\mathrm{ICB}}^{density}\right)^{\gamma}$, where $\gamma = 1.5$ is the Grüneisen parameter (Vočadlo et al., 2003), $\rho_{\mathrm{CMB}}^{density} = 9.90349$ g/cm^3 and $\rho_{\mathrm{ICB}}^{density} = 12.16634$ g/cm^3 are densities at the CMB and the ICB, respectively (Dziewonsk and Anderson, 1981). The present-day CMB temperature is plotted in Fig. 6 (a).

Next, we calculated the Si content, y, based on the comparison between the PREM density and that calculated from the EoS of $Fe_{1-y}Si_yH_x$ alloy at the CMB pressure and temperature (Fig. 5). Assuming that the volume increase $x\Delta V_H$ depends only on pressure, and independent of temperature and Si content, we formulated the EoS of $Fe_{1-y}Si_yH_x$ alloy to be $P_{Fe\text{-}Si\text{-}H}(V, T, x, y) = P_{Fe\text{-}Si}(V - x\Delta V_H, T, y)$. Following Tateno et al. (2015), the EoS of $Fe_{1-y}Si_y$ alloy is obtained by linear interpolation between the EoS of hcp Fe (Dewaele et al., 2006) and that of hcp Fe + 9wt.% Si alloy (Tateno et al., 2015). The $x\Delta V_H$ is calculated from EoS of hcp FeH_x of this study. Fig 6 (b) represents the Si content as a function of the H content. The Si content decreases with increasing the H content, as expected. Because of the convection, the composition is uniform throughout the outer core. The calculated density profiles of all compositions considered here are broadly consistent with the PREM at deep portion of the outer core (Fig. 5).

Then, we modeled the thermal conductivity of the ternary alloy. Similar to the model used by Gomi et al. (2016), we adopted the following core resistivity model with the resistivity saturation, which is proposed by Cote and Meisel (1978)

$$\rho_{tot}(V,T) = \left(1 - \frac{\rho_{tot}(V,T)}{\rho_{sat}(V)}\right)\rho_{ph,ideal}(V,T) + \rho_{imp}(V,y)\exp(-2W(V,T)) \quad (5)$$

where $\rho_{tot}(V, T)$ is the total resistivity, $\rho_{sat}(V)$ is the saturation resistivity, $\rho_{ph,ideal}(V, T)$ is the "ideal" phonon-contributed resistivity which neglects the effect of the resistivity saturation, $\rho_{imp}(V\ y)$ is the impurity resistivity at zero Kelvin, and $\exp(-2W(T))$ is the Debye-Waller factor which gives temperature coefficient of impurity resistivity. We must emphasize the absence of the magnetic scattering term in Eq (5). For the ferromagnetic body-centered cubic (bcc) Fe, the magnetic scattering resistivity is about double of the phonon contributed resistivity at 1 bar and at the Curie temperature

(Bäcklund, 1961). The experimentally measured total resistivity of ferromagnetic dhcp FeH at ~6 GPa (Antonov et al., 1982; 2002) shows a high resistance. The resistance ratio is R/R_0 ~ 9 at 330 ℃, where the subscript 0 indicates the ambient conditions. Assuming $\rho = \rho_0 R/R_0$ and $\rho_0 = 1.0 \times 10^{-7}$ Ωm, the estimated resistivity is ~ 9×10^{-7} Ωm, which is comparable to that of bcc Fe. The present calculations on the band structure of the LMD dhcp FeH_x show strong broadenings (Fig. 4), which imply a large magnetic scattering resistivity, consistent with the results of Antonov et al. (1982; 2002). If such magnetic moments are not quenched at the Earth's core condition, the magnetic scattering resistivity should have a large contribution to the total resistivity. However, our total energy calculations indicate that the stability field of ferromagnetic FeH_x is limited below ~ 65 GPa, suggesting the absence of magnetic scattering at the Earth's core, whose pressure range is above 135 GPa. We also neglected the effect of electron-electron correlations, which may not be significant (Pourovskii et al., 2014). The saturation resistivity is assumed to be propositional to $V^{1/3}$ (Gomi et al., 2013)

$$\rho_{\mathrm{sat}}(V) = \rho_{\mathrm{sat}}(V_0)\left(\frac{V}{V_0}\right)^{\frac{1}{3}} \tag{6}$$

where $\rho_{\mathrm{sat}}(V_0)$ = 1.68×10^{-6} Ωm is the saturation resistivity at 1 bar obtained from resistivity measurements on bcc and fcc Fe-based alloys (Bohnenkamp et al., 2002). We assumed that the phonon-contributed resistivity of dhcp FeH_x is very close to that of hcp Fe, which can be extrapolated from 300 K measurements of hcp Fe reported by Gomi et al. (2013). At around 300 K, the resistivity can be calculated by using the Bloch-Grüneisen formula,

$$\rho_{\mathrm{ph,ideal}}(V,T) = B(V)\left(\frac{T}{\Theta_D(V)}\right)^5 \int_0^{\Theta_D(V)/T} \frac{z^5 \mathrm{d}z}{(\exp(z) - 1)(1 - \exp(-z))} \tag{7}$$

where $B(V)$ is the material constant (Gomi et al., 2013) and $\Theta_D(V)$ is the Grüneisen parameter (Dewaele et al., 2006). The Bloch-Grüneisen formula can reproduce the temperature dependence of hcp Fe up to 450 K (Gomi et al., 2013; Ohta et al., 2016). However, it will be violated because of the resistivity saturation, and the total resistivity of pure metals can reasonably be represented by the Shut-resistor model (Wiesmann et al. 1977).

$$\frac{1}{\rho_{tot}(V,T)} = \frac{1}{\rho_{ph,ideal}(V,T)} + \frac{1}{\rho_{sat}(V)} \quad (8)$$

Note that, if we ignore the impurity resistivity, Eq (5) is equivalent to the Shut-resistor model (Eq 8).

It is still being discussed the amount and the composition of light alloying elements in the Earth's Fe-Ni dominant core. The presence of the impurity elements causes an additional scattering of electron in metal, which is the origin of impurity resistivity. For the impurity resistivity in the core, the effect of alloying Si has been most widely investigated (Mattasov, 1977; Stacey and Anderson, 2001; Seagle et al., 2013; Gomi et al., 2013; 2016; Kiarasi and Secco, 2015). Gomi et al. (2016) suggested that the Si impurity resistivity is larger than the phonon-contributed resistivity and the Ni impurity resistivity for the hypothetical Fe-Ni-Si composition. This inversely implies that, if the actual light elements have smaller impurity resistivity than Si impurity, the estimated total resistivity should largely be decreased. In this study, it is found that almost no broadening of the band structure in the vicinity of the Fermi energy due to the H disorder effect, which qualitatively indicates no H impurity resistivity. Therefore, we assumed that the impurity resistivity depends only on the Si content. The CMB value is interpolated from the first-principles results at V =16.27 Å reported by Gomi et al. (2016). Assuming the Debye model, $W(T)$ can be obtained as follows (Markowitz,

1976)

$$W(T) = \frac{3\eta^2 K^2 T^2}{2mk_B\Theta_D^3}\int_0^{\Theta_D/T}\left(\frac{1}{\exp(z)-1}+\frac{1}{2}\right)z\mathrm{d}z \quad (9)$$

where $\hbar$ is the reduced Planck's constant (the Dirac's constant), k_B is the Boltzmann constant, m is the atomic mass, and K is electronic wave vector transfer. Although it decreases the impurity resistivity with increasing temperature, the Debye-Waller factor exp(-2W(T)) is very close to unity in general (Rossiter, 1978; Markowitz, 1976) and can be negligible even at the Earth's core temperature condition (Gomi et al., 2016). Usually, the resistivity of metals increases upon melting, however, its magnitude is basically small for transition metals (Faber, 1972). The resistivity enhancement is ~ 8% for Fe at 1 bar (Van Zytveld, 1980) and 7 GPa (Secco and Schloessin, 1989). Recently, Wagle and Steinle-Neumann (2018) suggested that the resistivity change decreases with pressure and to be negligibly small at the inner core boundary. This situation is also valid for the thermal conductivity (Nishi et al., 2003). Therefore, we simply ignored this effect. The thermal conductivity was then estimated from the Wiedemann-Franz law, $k = LT/\rho_{\mathrm{tot}}$ where k is the thermal conductivity, and L is the Lorenz number. Applying the Sommerfeld expansion, the Lorenz number is estimated to L_{Somm} = 2.45 × 10^{-8} $\mathrm{W\Omega K^{-2}}$ (Gomi and Hirose, 2015). This could be potentially violated, which yields about 40 % of the maximum uncertainty (Gomi and Hirose, 2015; Secco, 2017). However, we used the Sommerfeld value of the Lorenz number as a representative value. Fig 6 (c) shows the present-day conductivity at the top of the outer core. The effect of H alloying causes the reduction of melting temperature and electrical resistivity. These two factors, which have opposite contribution to the thermal conductivity, are almost cancelled out. Therefore, the thermal conductivity is ~ 100 W/m/K, which is almost constant versus H

content. The estimated thermal conductivity is comparable to the high values obtained from recent theoretical and experimental studies (Pozzo et al., 2012; de Koker et al., 2012; Ohta et al., 2016; Gomi and Hirose, 2015; Gomi et al., 2013; 2016).

Finally, we solved the energy conservation equations of the core to calculate the thermal history of the Earth's core (Labrosse, 2015; Gomi et al., 2013, 2016; see also Supplementary text). We assumed that the CMB heat flow is always equal to the isentropic heat flow at the CMB, which maximize the inner core age. We did not consider any contribution from radioactive elements. The calculated maximum inner core age is 0.49 Gyr at $x = 0$, whereas it increases to 0.86 Gyr at $x = 0.7$ (Fig 6 d). This is because the incorporation of hydrogen contributes to the reduction of the core temperature, which decreases the core adiabatic temperature gradient (Gomi and Hirose, 2015). Previous estimates of the inner core age are highly uncertain. The high value of thermal conductivity (c.a. ~ 100 W/m/K) indicates young inner core (< 1 Gyr) (e.g. Gomi et al., 2013; 2016; Gomi and Hirose, 2015; Ohta et al., 2016; Pozzo et al. 2012; de Koker et al., 2012), whereas the low value (c.a. ~ 30 W/m/K) allows much older inner core (~ 3 Gyr) (Stacey and Loper, 2007; Konopkova et al., 2016). Even though the effects of hydrogen increase the maximum inner core age, our new value of young inner core age is inconsistent with the Mesoproterozoic (~1.3 Ga) inner core nucleation proposed by Bigin et al. (2015). Reconciliation of the difference requires further examination of the palaeomagnetic intensity data (Smirnov et al., 2016) and assessment of energy budget in early history of the Earth.

The effect of ferromagnetism may play an important role in smaller planets and satellites, if their iron-dominant cores contain hydrogen. For example, such a situation likely occurs at the interior of the Ganymede, which contains large amount of hydrogen

426 as the thick icy mantle, and hence, coexisting iron may react to form iron hydrides
427 (Fukai, 1984; Okuchi, 1997; Yagi and Hishinuma 1995; Shibazaki et al., 2011; Terasaki
428 et al., 2012). Our prediction of the Curie temperature of dhcp $FeH_{1.0}$ is comparable to
429 the temperature of interior of these smaller bodies (e.g. Kimura et al., 2009). If the
430 internal temperature is below the Curie temperature, the FeH_x alloy has spontaneous
431 magnetism and could be a source of remnant magnetism of the bodies (e.g. Crary and
432 Bagenal, 1998). Note that the electron band structure of LMD state is significantly
433 different from that of non-magnetic phase, which also emphasizes the importance of
434 ferromagnetism, even if the internal temperature is above the Curie temperature.

435 **ACKNOWLEDGMENTS**

436 Postdoctoral fellowship to H.G. is supported by the NASA (NNX14AG26G) and NSF
437 (EAR-1214990) grants to Y.F. This work was also supported by JSPS
438 MEXT/KAKENHI Grant Number JP15H05827. We thank two anonymous reviewers
439 for their constructive comments and suggestions.
440

REFERENCES CITED

Akai, H. (1989) Fast Korringa-Kohn-Rostoker coherent potential approximation and its application to FCC Ni-Fe systems, Journal of Phyisics: Condenced Matter, 1(43), 8045-8063.

Akai, H., and Dederichs, P. H. (1993) Local moment disorder in ferromagnetic alloys, Physical Revew B, 47(14), 8739-8747.

Alfè, D. (2009). Temperature of the inner-core boundary of the Earth: Melting of iron at high pressure from first-principles coexistence simulations. Physical Review B, 79(6), 060101.

Antonov, V. E., Belash, I. T., and Ponyatovsky, E. G. (1982). T-P phase diagram of the Fe-H system at temperatures to 450 ℃ and pressures to 6.7 GPa. Scripta Metallurgica, 16(2), 203-208.Antonov, V. E., Cornell, K., Fedotov, V. K., Kolesnikov, A. I., Ponyatovsky, E. G., Shiryaev, V. I., and Wipf, H. (1998) Neutron diffraction investigation of the dhcp and hcp iron hydrides and deuterides. Journal of Alloys and Compounds, 264(1), 214-222.

Antonov, V., Baier, M., Dorner, B., Fedotov, V., Grosse, G., Kolesnikov, A., Ponyatovsky, E., Schneider, G., and Wagner, F. (2002) High-pressure hydrides of iron and its alloys, Journal of Physics: Condenced Matter, 14(25), 6427-6445.

Anzellini, S., Dewaele, A., Mezouar, M., Loubeyre, P., and Morard, G. (2013). Melting of iron at Earth's inner core boundary based on fast X-ray diffraction. Science, 340(6131), 464-466.

Biggin, A. J., Piispa, E. J., Pesonen, L. J., Holme, R., Paterson, G. A., Veikkolainen, T., and Tauxe, L. (2015) Palaeomagnetic field intensity variations suggest Mesoproterozoic inner-core nucleation. Nature, 526(7572), 245-248.

Birch, F. (1964) Density and composition of mantle and core, Journal of Geophysical Research, 69(20), 4377-4388.

Bohnenkamp, U., Sandström, R., and Grimvall, G. (2002). Electrical resistivity of steels and face-centered-cubic iron. Journal of Applied Physics, 92(8), 4402-4407.

Caracas, R. (2015) The influence of hydrogen on the seismic properties of solid iron, Geophysical Research Letters, 42(10), 3780-3785.

Crary, F. J., and Bagenal, F. (1998) Remanent ferromagnetism and the interior structure of Ganymede, Journal of Geophysical Research, 103(E11), 25757-25773.

Cote, P. J., and Meisel, L. V. (1978). Origin of saturation effects in electron transport. Physical Review Letters, 40(24), 1586-1589.

de Koker, N., Steinle-Neumann, G., and Vlček, V. (2012) Electrical resistivity and thermal conductivity of liquid Fe alloys at high P and T, and heat flux in Earth's core. Proceedings of the National Academy of Sciences of the United States of America, 109(11), 4070-4073.

Dewaele, A., Loubeyre, P., Occelli, F., Mezouar, M., Dorogokupets, P. I., and Torrent, M., (2006) Quasihydrostatic equation of state of iron above 2 Mbar, Physical Review Letters, 97(21), 215504.

Drchal, V., Kudrnovský, J., Wagenknecht, D., Turek, I., and Khmelevskyi, S. (2017). Transport properties of iron at Earth's core conditions: The effect of spin disorder. Physical Review B, 96(2), 024432.

Dziewonski, A. M., and Anderson, D. L. (1981). Preliminary reference Earth model. Physics of the Earth and Planetary Interiors, 25(4), 297-356.

Ebert, H., Mankovsky, S., Chadova, K., Polesya, S., Minár, J., and Ködderitzsch, D. (2015) Calculating linear-response functions for finite temperatures on the basis of

489 the alloy analogy model, Physical Revew B, 91(16), 165132.
490 Elsässer, C., Zhu, J., Louie, S., Meyer, B., and Chan, C. (1998) Ab initio study of iron
491 and iron hydride: II. Structural and magnetic properties of close-packed Fe and
492 FeH, Journal of Physics: Condenced Matter, 10(23), 5113-5129.
493 Faber, T. E. (1972) Introduction to the Theory of Liquid Metals. Cambridge at the
494 University Press.
495 Fei, Y. Murphy, C., Shibazaki, Y., Shahar, and A. Huang, H. (2016) Thermal equation of
496 state of hcp-iron: Constraint on the density deficit of Earth's solid inner core,
497 Geophysical Reseach Letters, 43(13), 6837-6843.
498 Fischer, R. A., Campbell, A. J., Reaman, D. M., Miller, N. A., Heinz, D. L., Dera, P.,
499 and Prakapenka, V. B. (2013). Phase relations in the Fe–FeSi system at high
500 pressures and temperatures. Earth and Planetary Science Letters, 373, 54-64.
501 Fukai, Y. (1984) The iron-water reaction and the evolution of the Earth, Nature 308,
502 174-175.
503 Fukai, Y. (1992) Some properties of the Fe–H system at high pressures and temperatures,
504 and their implications for the Earth’s core, High-pressure Research: Application to
505 Earth and Planetary Science, 373-385.
506 Fukai, Y. (2006) The metal-hydrogen system: basic bulk properties, Springer Science &
507 Business Media.
508 Glasbrenner, J. K., Pujari, B. S., and Belashchenko, K. D. (2014) Deviation from
509 Matthiessen’s rule and resistivity saturation effects in Gd and Fe from first
510 principles, Physical Review B, 89(16), 174498.
511 Gomi, H., and Hirose, K. (2015) Electrical resistivity and thermal conductivity of hcp
512 Fe–Ni alloys under high pressure: Implications for thermal convection in the

513 Earth’s core, Physics of the Earth and Planetary Interior, 247, 2-10.
514 Gomi, H., Hirose, K., Akai, H., and Fei, Y. (2016) Electrical resistivity of
515 substitutionally disordered hcp Fe–Si and Fe–Ni alloys: Chemically-induced
516 resistivity saturation in the Earth's core, Eart and Planetery Science Letters, 451,
517 51-61.
518 Gomi, H., Ohta, K., Hirose, K., Labrosse, S., Caracas, R., Verstraete, M. J., and
519 Hernlund, J. W. (2013) The high conductivity of iron and thermal evolution of the
520 Earth’s core, Physcs of Earth and Planetery Interior, 224, 88-103.
521 Hirao, N., Kondo, T., Ohtani, E., Takemura, K., and Kikegawa, T. (2004) Compression
522 of iron hydride to 80 GPa and hydrogen in the Earth's inner core, Geophyscal
523 Research Letters, 31(6), L06616.
524 Iizuka-Oku, R., Yagi, T., Gotou, H., Okuchi, T., Hattori, T., and Sano-Furukawa, A.
525 (2017) Hydrogenation of iron in the early stage of Earth's evolution. Nature
526 communications, 8, 14096.
527 Isaev, E. I., Skorodumova, N. V., Ahuja, R., Vekilov, Y. K., and Johansson, B. (2007)
528 Dynamical stability of Fe-H in the Earth's mantle and core regions, Proceedings of
529 the Natinal Academy of Sciences of the United States of America, 104(22),
530 9168-9171.
531 Kiarasi, S., and Secco, R. A. (2015). Pressure - induced electrical resistivity saturation
532 of Fe17Si. physica status solidi (b), 252(9), 2034-2042.
533 Kimura, J., Nakagawa, T., and Kurita, K. (2009) Size and compositional constraints of
534 Ganymede's metallic core for driving an active dynamo. Icarus, 202(1), 216-224.
535 Konôpková, Z., McWilliams, R. S., Gómez-Pérez, N., and Goncharov, A. F. (2016)
536 Direct measurement of thermal conductivity in solid iron at planetary core

conditions, Nature, 534(7605), 99-101.

Labrosse, S. (2015) Thermal evolution of the core with a high thermal conductivity. Physics of the Earth and Planetary Interior, 247, 36-55.

Machida, A., Saitoh, H., Sugimoto, H., Hattori, T., Sano-Furukawa, A., Endo, N., Katayama, Y., Iizuka, R., Sato, T., Matsuo, M., Orimo, S., and Aoki, K. (2014) Site occupancy of interstitial deuterium atoms in face-centred cubic iron, Nature communications., 5, 5063.

Mao, W. L., Sturhahn, W., Heinz, D. L., Mao, H. K., Shu, J., and Hemley, R. J. (2004) Nuclear resonant x−ray scattering of iron hydride at high pressure, Geophysical Research Letters, 31(15), L15618.

Markowitz, D., (1977). Calculation of electrical resistivity of highly resistive metallic alloys. Physical Revew B 15, 3617-3619.

Matassov, G., (1977), The electrical conductivity of iron-silicon alloys at high pressures and the Earth's core. PhD thesis, Lawrence Livermore Lab., Univ. California.

Matsuoka, T., Hirao, N., Ohishi, Y., Shimizu, K., Machida, A., and Aoki, K. (2011) Structural and electrical transport properties of FeH_x under high pressures and low temperatures, High Pressure Research, 31(1), 64-67.

Mitsui, T., and Hirao, N. (2010) Ultrahigh-pressure study on the magnetic state of iron hydride using an energy domain synchrotron radiation ^{57}Fe Mössbauer spectrometer, Materials Research Society Symposium Online Proceedings Library, 1262, 115-119.

Narygina, O., Dubrovinsky, L. S., McCammon, C. A., Kurnosov, A., Kantor, I. Y., Prakapenka, V. B., and Dubrovinskaia, N. A. (2011) X-ray diffraction and Mössbauer spectroscopy study of fcc iron hydride FeH at high pressures and

561 implications for the composition of the Earth's core, Earth and Planetary Science
562 Letters, 307(3), 409-414.
563 Nishi, T., Shibata, H., Ohta, H., and Waseda, Y. (2003) Thermal conductivities of molten
564 iron, cobalt, and nickel by laser flash method. Metallurgical and Materials
565 Transactions A, 34, 2801-2807.
566 Ohta, K., Kuwayama, Y., Hirose, K., Shimizu, K., and Ohishi, Y. (2016) Experimental
567 determination of the electrical resistivity of iron at Earth’s core conditions. Nature,
568 534(7605), 95-98.
569 Okuchi, T. (1997) Hydrogen partitioning into molten iron at high pressure: implications
570 for Earth's core. Science, 278(5344), 1781-1784.
571 Okuchi, T., (1998). The melting temperature of iron hydride at high pressures and its
572 implications for the temperature of the Earth's core, Journal of Physics: Condenced
573 Matter, 10(49), 11595-11598.
574 Pépin, C. M., Dewaele, A., Geneste, G., Loubeyre, P., and Mezouar, M. (2014) New
575 iron hydrides under high pressure, Physical Review Letters, 113(26), 265504.
576 Perdew, J. P., Burke, K., and Ernzerhof, M. (1996) Generalized gradient approximation
577 made simple, Physical Review Letters, 77(18), 3865-3868.
578 Pourovskii, L. V., Mravlje, J., Ferrero, M., Parcollet, O., and Abrikosov, I. A. 2014.
579 Impact of electronic correlations on the equation of state and transport in ε-Fe.
580 Physical Review B, 90(15), 155120.
581 Pozzo, M., Davies, C., Gubbins, D., and Alfe, D. (2012) Thermal and electrical
582 conductivity of iron at Earth/'s core conditions. Nature, 485(7398), 355-358.
583 Rossiter, P.L., 1987. The electrical resistivity of metals and alloys. Cambridge
584 University Press.

585 Sakamaki, K., Takahashi, E., Nakajima, Y., Nishihara, Y., Funakoshi, K., Suzuki, T., and
586 Fukai, Y., (2009) Melting phase relation of FeH_x up to 20GPa: Implication for the
587 temperature of the Earth's core, Physics of the Earth and Planetery Interior, 174(1),
588 192-201.
589 Sato, K., Dederics, P., and Katayama-Yoshida, H., (2003) Curie temperatures of III–V
590 diluted magnetic semiconductors calculated from first principles, Europhysics
591 Letters, 61(3), 403-408.
592 Schneider, G., Baier, M., Wordel, R., Wagner, F. E., Antonov, V. E., Ponyatovsky, E. G.,
593 Kopilovskii, Y., and Makarov, E. (1991) Mössbauer study of hydrides and
594 deuterides of iron and cobalt. Journal of the Less Common Metetals, 172,
595 333-342.
596 Seagle, C. T., Cottrell, E., Fei, Y., Hummer, D. R., and Prakapenka, V. B. (2013)
597 Electrical and thermal transport properties of iron and iron−silicon alloy at high
598 pressure. Geophysical Research Letters, 40(20), 5377-5381.
599 Secco, R. A. 2017. Thermal conductivity and Seebeck coefficient of Fe and Fe-Si
600 alloys: Implications for variable Lorenz number. Physics of Earth and Planetery
601 Interior, 265, 23-34.
602 Secco, R.A., Schloessin, H.H., 1989. The electrical resistivity of solid and liquid Fe at
603 pressure up to 7 GPa. Journal of Geophysical Research 94, 5887-5894.
604 Shibazaki, Y., Ohtani, E., Fukui, H., Sakai, T., Kamada, S., Ishikawa, D., Tsutsui, S.,
605 Baron, A. Q., Nishitani, N., and Hirao, N. (2012) Sound velocity measurements in
606 dhcp-FeH up to 70GPa with inelastic X-ray scattering: Implications for the
607 composition of the Earth's core, Earth and Planetary Science Letters, 313, 79-85.
608 Shibazaki, Y., Ohtani, E., Terasaki, H., Tateyama, R., Sakamaki, T., Tsuchiya, T., and

609 Funakoshi, K. I. (2011) Effect of hydrogen on the melting temperature of FeS at
610 high pressure: Implications for the core of Ganymede, Earth and Planetary Science
611 Letters, 301(1-2). 153-158
612 Shibazaki, Y., Terasaki, H., Ohtani, E., Tateyama, R., Nishida, K., Funakoshi, K., and
613 Higo, Y., (2014) High-pressure and high-temperature phase diagram for
614 $Fe_{0.9}Ni_{0.1}$-H alloy, Physics of the Earth and Planetary Interior 228, 192-201.
615 Shiga, M. (1974) Correlation between lattice constant and magnetic moment in 3d
616 transition metal alloys, AIP Conference Proceedings, 18(1), 463-477.
617 Smirnov, A. V., Tarduno, J. A., Kulakov, E. V., McEnroe, S. A., and Bono, R. K. (2016)
618 Palaeointensity, core thermal conductivity and the unknown age of the inner core.
619 Geophysical Journal International, 205(2), 1190-1195.
620 Stacey, F. D., and Anderson, O. L. (2001). Electrical and thermal conductivities of Fe–
621 Ni–Si alloy under core conditions. Physics of the Earth and Planetary Interiors,
622 124(3-4), 153-162.
623 Stacey, F. D., and Loper, D. E. (2007). A revised estimate of the conductivity of iron
624 alloy at high pressure and implications for the core energy balance. Physics of the
625 Earth and Planetary Interiors, 161(1-2), 13-18.
626 Suehiro, S., Ohta, K., Hirose, K., Morard, G., and Ohishi, Y. (2017) The influence of
627 sulfur on the electrical resistivity of hcp iron: Implications for the core conductivity
628 of Mars and Earth. Geophysical Research Letters, 44,
629 Sugimoto, H., and Fukai, Y. (1992) Solubility of hydrogen in metals under high
630 hydrogen pressures: thermodynamical calculations. Acta Metallurgica et Materialia,
631 40(9), 2327-2336.
632 Tagawa, S., Ohta, K., Hirose, K., Kato, C., and Ohishi, Y. (2016) Compression of Fe–

633 Si–H alloys to core pressures, Geophysical Research Letters, 43(8), 3686-3692.
634 Tateno, S., Kuwayama, Y., Hirose, K., and Ohishi, Y. (2015). The structure of Fe–Si
635 alloy in Earth's inner core. Earth and Planetary Science Letters, 418, 11-19.
636 Terasaki, H., Ohtani, E., Sakai, T., Kamada, S., Asanuma, H., Shibazaki, Y., Hirao, N.,
637 Sata, N., Ohishi, Y., Sakamaki, T., Suzuki, A., and Funakoshi, K. (2012) Stability
638 of Fe–Ni hydride after the reaction between Fe–Ni alloy and hydrous phase
639 (δ-AlOOH) up to 1.2 Mbar: Possibility of H contribution to the core density deficit.
640 Physics of the Earth and Planetery Interior, 194-195, 18-24.
641 Tsumuraya, T., Matsuura, Y., Shishidou, T., and Oguchi, T. (2012) First-principles study
642 on the structural and magnetic properties of iron hydride, Journal of Physical
643 Society of Japan., 81(6), 064707.
644 Umemoto, K., and Hirose, K. (2015) Liquid iron-hydrogen alloys at outer core
645 conditions by first-principles calculations, Geophysical Research Letters, 42(18),
646 7513-7520.
647 Van Zytveld, J. B. (1980). Electrical resistivities of liquid transition metals. Le Journal
648 de Physique Colloques, 41(C8), C8-503.
649 Vočadlo, L., Alfe, D., Gillan, M. J., and Price, G. D. (2003). The properties of iron
650 under core conditions from first principles calculations. Physics of the Earth and
651 Planetary Interiors, 140(1-3), 101-125.
652 Wagle, F., and Steinle-Neumann, G. (2018) Electrical resistivity discontinuity of iron
653 along the melting curve. Gephysical Journal International, 213, 237-243.
654 Wiesmann, H., Gurvitch, M., Lutz, H., Gohsh, A, Schwarz, B., Strongin, M., Allen, P.B.,
655 and Halley, J.W. 1977. Simple model for characterizing the electrical resistivity in
656 A-15 superconductors. Physical Review. Letters. 38, 782-785.

Yagi, T., and Hishinuma, T. (1995). Iron hydride formed by the reaction of iron, silicate, and water: Implications for the light element of the Earth's core. Geophysical Research Letters, 22(14), 1933-1936.

Yamakata, M., Yagi, T., Utsumi, W., and Fukai, Y. (1992) In situ X-ray observation of iron hydride under high pressure and high temperature, Proceedings of the Japan Academy, Series B, 68(10), 172-176.

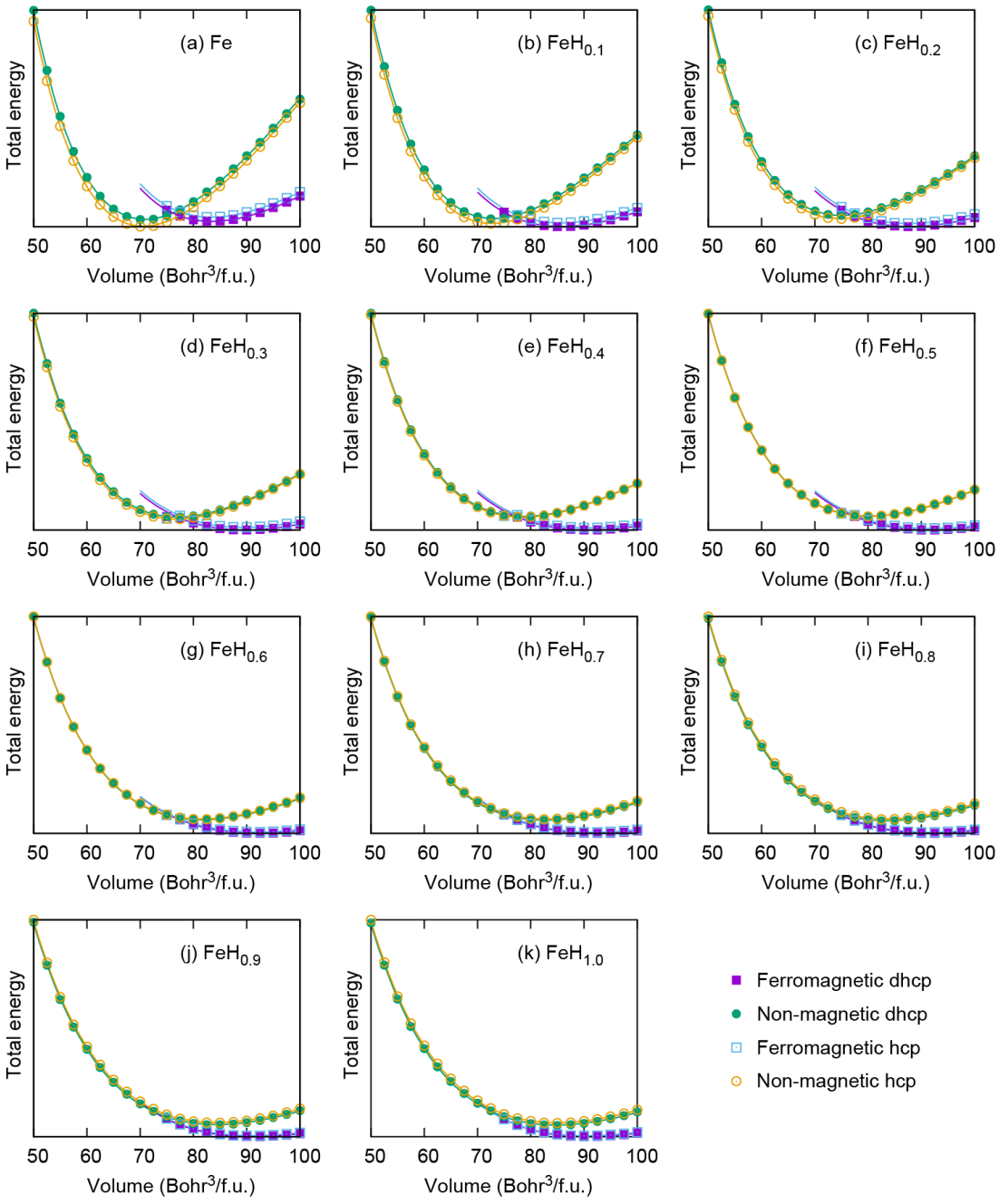

665

666 **Fig. 1.** Total energy of hcp and dhcp FeH_x with ferromagnetic and non-magnetic spin
667 alignment, where x is hydrogen content (filled square: ferromagnetic dhcp, filled circle:
668 non-magnetic dhcp, open square: ferromagnetic hcp, open circle: non-magnetic hcp).
669

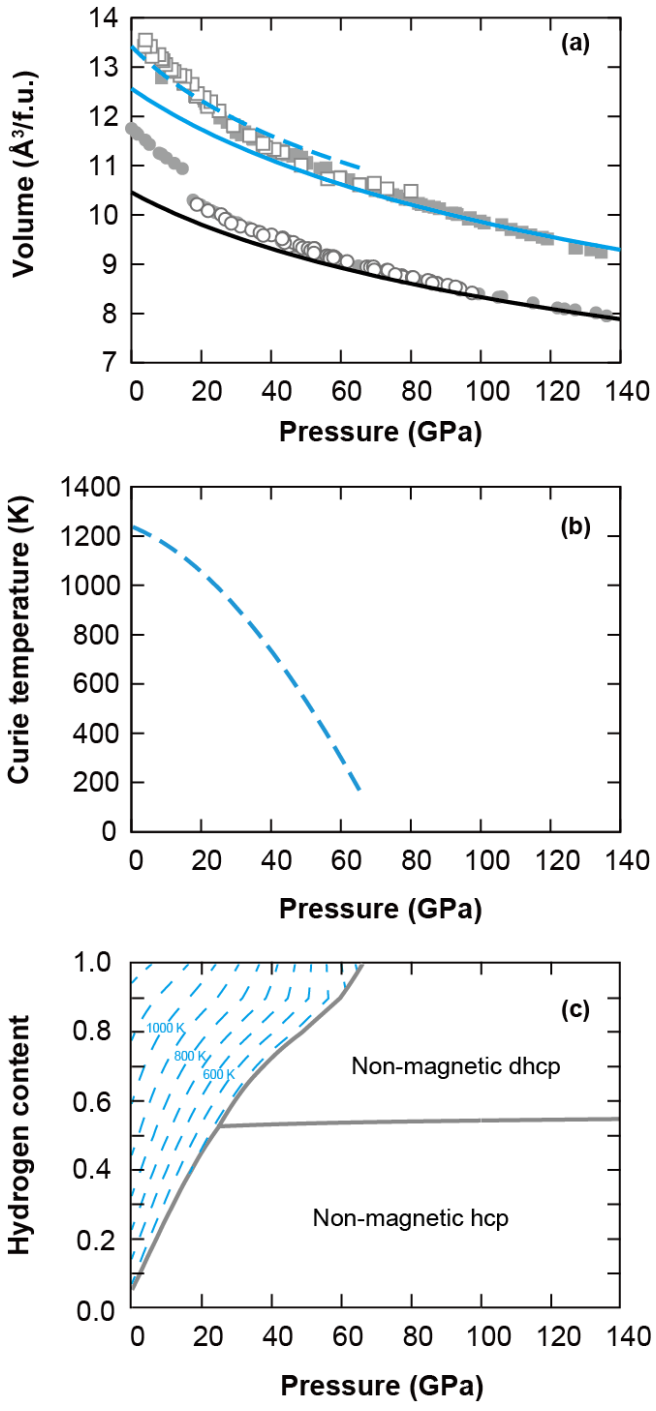

670

671 **Fig. 2.** (a) Compression curves of dhcp FeH and hcp Fe. Blue broken line indicates
672 ferromagnetic dhcp FeH. Blue and black solid lines are non-magnetic dhcp FeH and hcp
673 Fe, respectively. Previous DAC measurements (open square; Hirao et al. (2004), filled

674 square: Pépin et al. (2014), open circle: Fei et al. (2016), filled circle: Dewaele et al.
675 (2006)) are also shown for comparison. (b) Curie temperature of dhcp FeH. (c) Stable
676 crystal and magnetic structure of FeH_x as function of pressure at given hydrogen content.
677 Note that we only considered following four phases: ferromagnetic dhcp, nonmagnetic
678 dhcp, ferromagnetic hcp and nonmagnetic hcp. We also neglect the phase separation,
679 which may occur at low temperature.
680

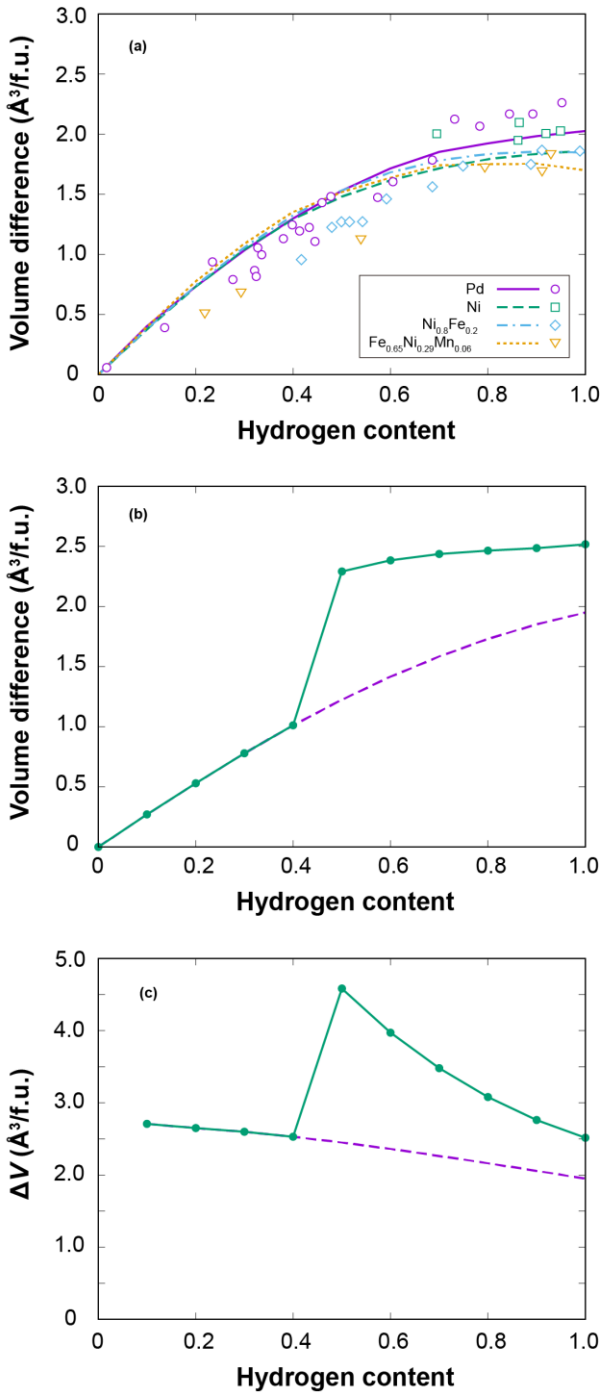

681

682 **Fig. 3.** Increase of volume of metal-hydrogen alloys as functions of hydrogen content, *x*.
683 (a) fcc metal-hydrogen alloys at ambient pressure. Our first-principles results (purple
684 solid line: Pd, green dashed line: Ni, blue dotted-dashed line: $Ni_{0.8}Fe_{0.2}$, yellow dotted

line: $Fe_{0.65}Ni_{0.29}Mn_{0.06}$) are consistent with previous experiments (purple circle: Pd, green square: Ni, blue diamond: $Ni_{0.8}Fe_{0.2}$, yellow triangle: $Fe_{0.65}Ni_{0.29}Mn_{0.06}$) (Fukai, 2006). (b) FeH_x alloys at 20 GPa. Green solid line with circle indicates FeH_x of stable phase, whereas purple broken line represents FeH_x in non-magnetic state. Note that magnetic transition violates the linear volume-hydrogen content relation, which observed in nonmagnetic FeH_x and many fcc metal-hydrogen alloys. (c) The $\Delta V_H = (V_{FeHx} - V_{Fe}) / x$ of FeH_x at 20 GPa.

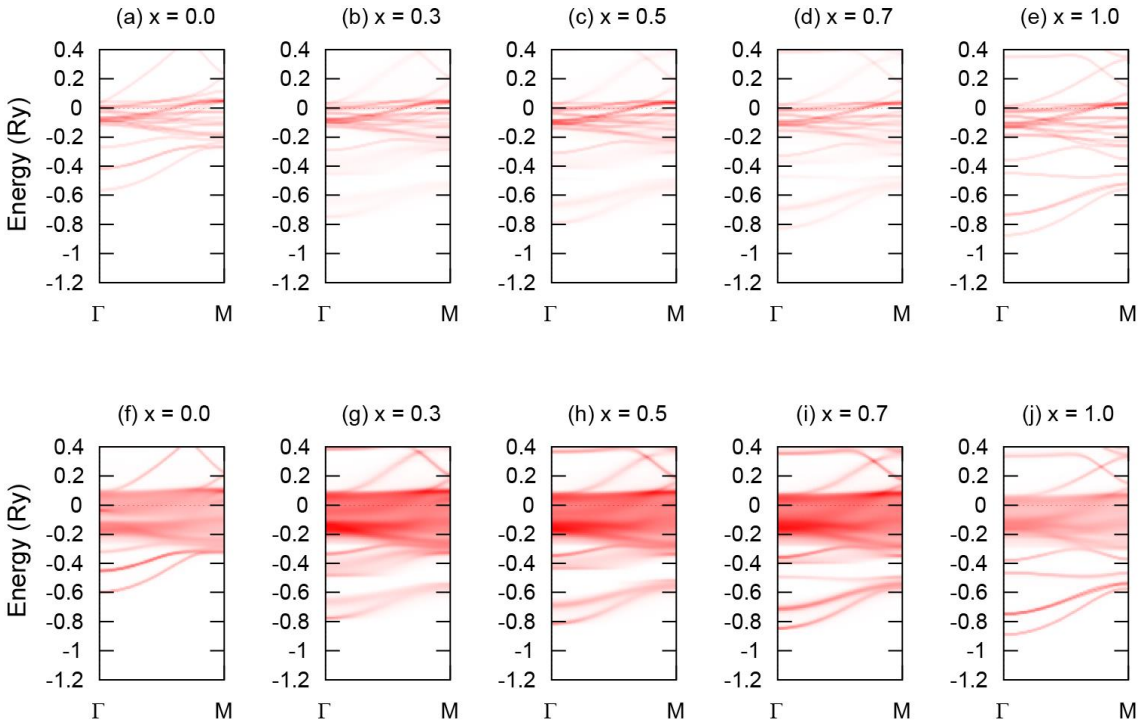

693

694 **Fig. 4**. Electronic band structures of dhcp FeH_x alloys at V = 90 $Bohr^3$/f.u. (a) to (e) are
695 non-magnetic states with x = 0.0, 0.3, 0.5, 0.7, and 1.0, respectively. Similarly, (f) to (j)
696 are LMD states. Note that the broadening due to the chemical disorder of interstitial
697 hydrogen is observed mainly at around -0.6 Ry, whereas the broadening due to the
698 magnetic disorder is significant at the vicinity of the Fermi level.

699

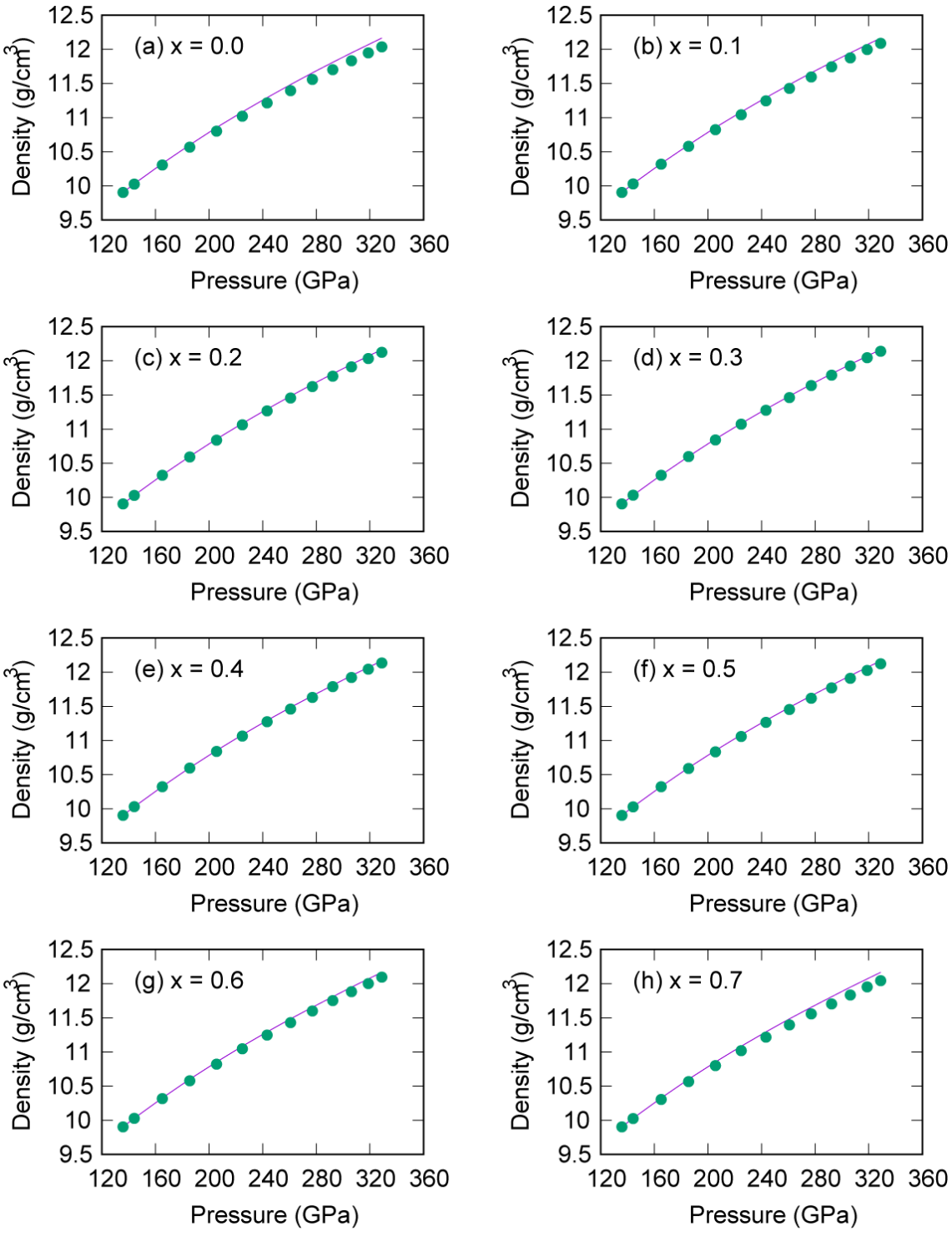

700

701 **Fig.5.** The PREM (green circle) and the calculated (purple line) density from the

702 equation of states of $Fe_{1-y}Si_yH_x$ alloys. The Si contents are determined so that the density

703 of the alloy match the density of PREM at the CMB.

704

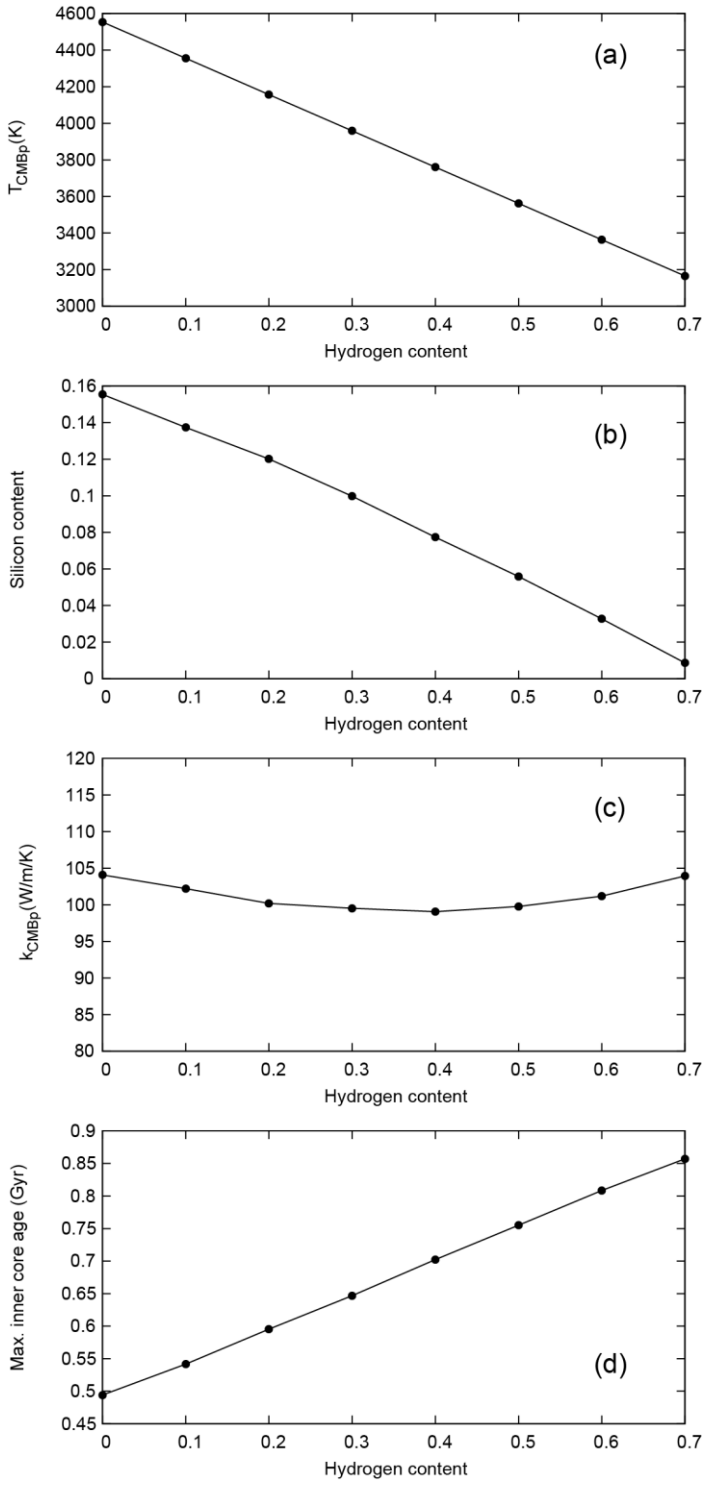

705

706 **Fig. 6.** Modeling results of $Fe_{1-y}Si_yH_x$ ternary core as function of hydrogen content, *x*.

707 (a) Present-day CMB temperature. (b) Silicon content, which match the PREM density

708 at the CMB. (c) Present-day CMB thermal conductivity. (d) Maximum inner core age.

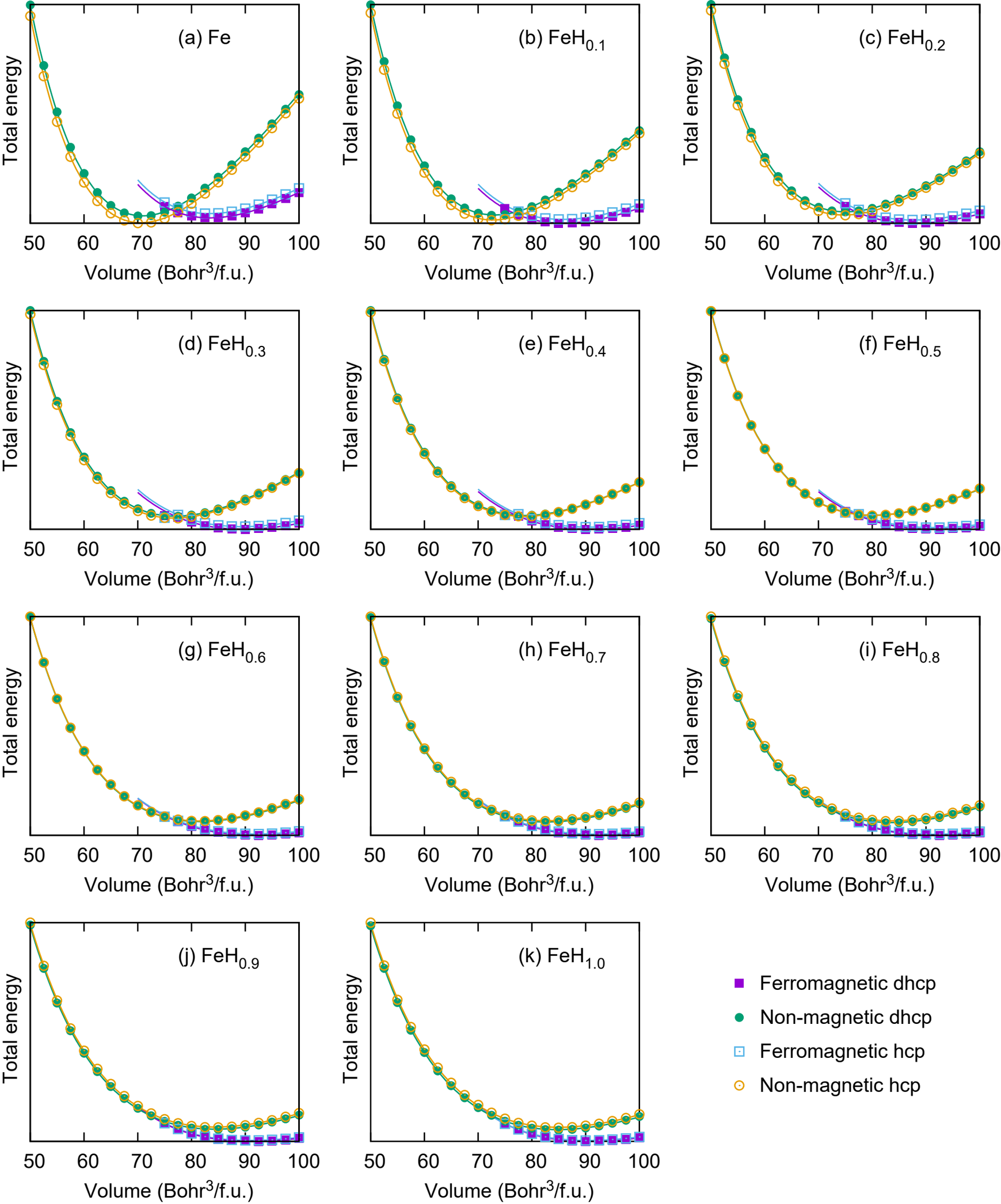
(a) Fe
(b) FeH0.1
(c) FeH0.2
(d) FeH0.3
(e) FeH0.4
(f) FeH0.5
(g) FeH0.6
(h) FeH0.7
(i) FeH0.8
(j) FeH0.9
(k) FeH1.0
Total energy
Volume (Bohr3/f.u.)
50
60
70
80
90
100
Ferromagnetic dhcp
Non-magnetic dhcp
Ferromagnetic hcp
Non-magnetic hcp

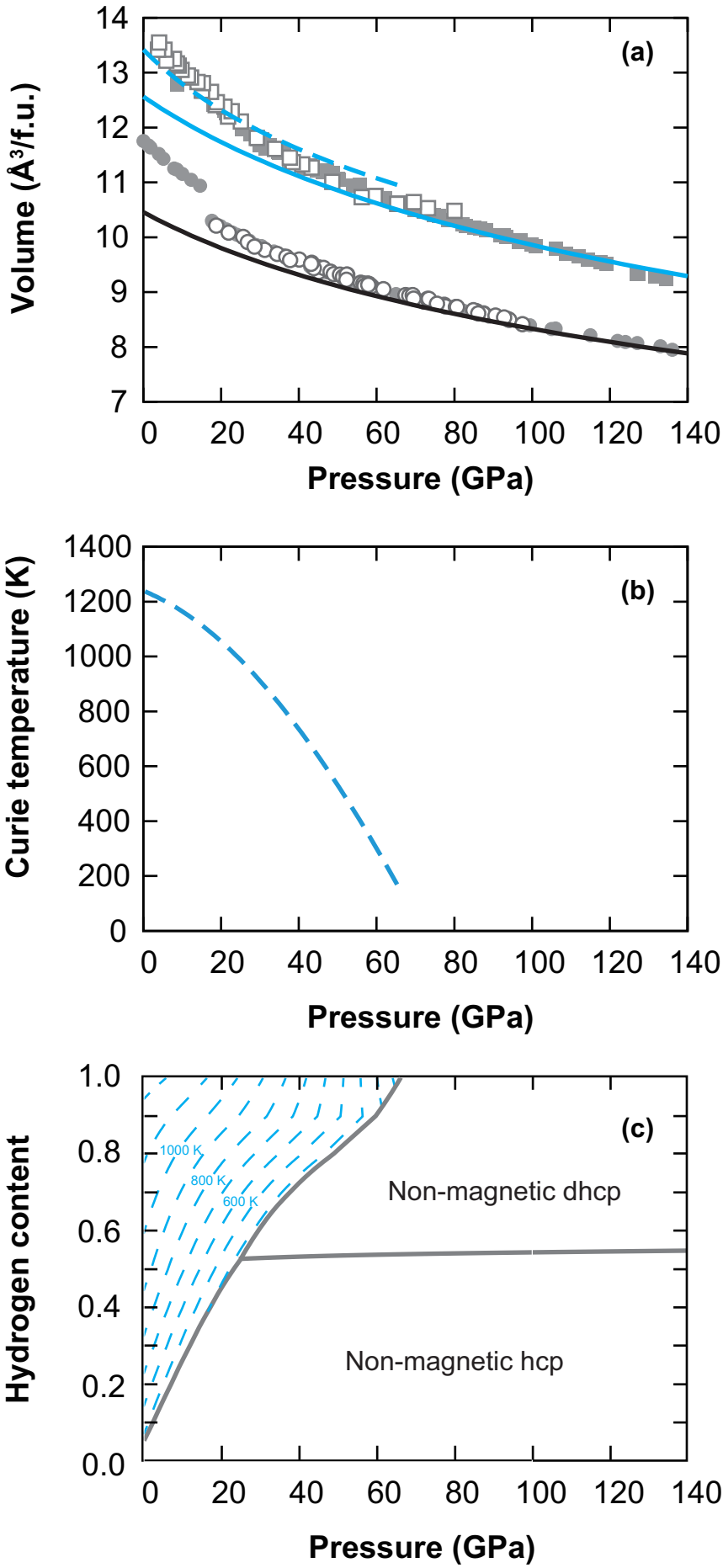
(a)
Volume (Å³/f.u.)
14
13
12
11
10
9
8
7
0
20
40
60
80
100
120
140
Pressure (GPa)
(b)
Curie temperature (K)
1400
1200
1000
800
600
400
200
0
0
20
40
60
80
100
120
140
Pressure (GPa)
(c)
Hydrogen content
1.0
0.8
0.6
0.4
0.2
0.0
1000 K
800 K
600 K
Non-magnetic dhcp
Non-magnetic hcp
0
20
40
60
80
100
120
140
Pressure (GPa)

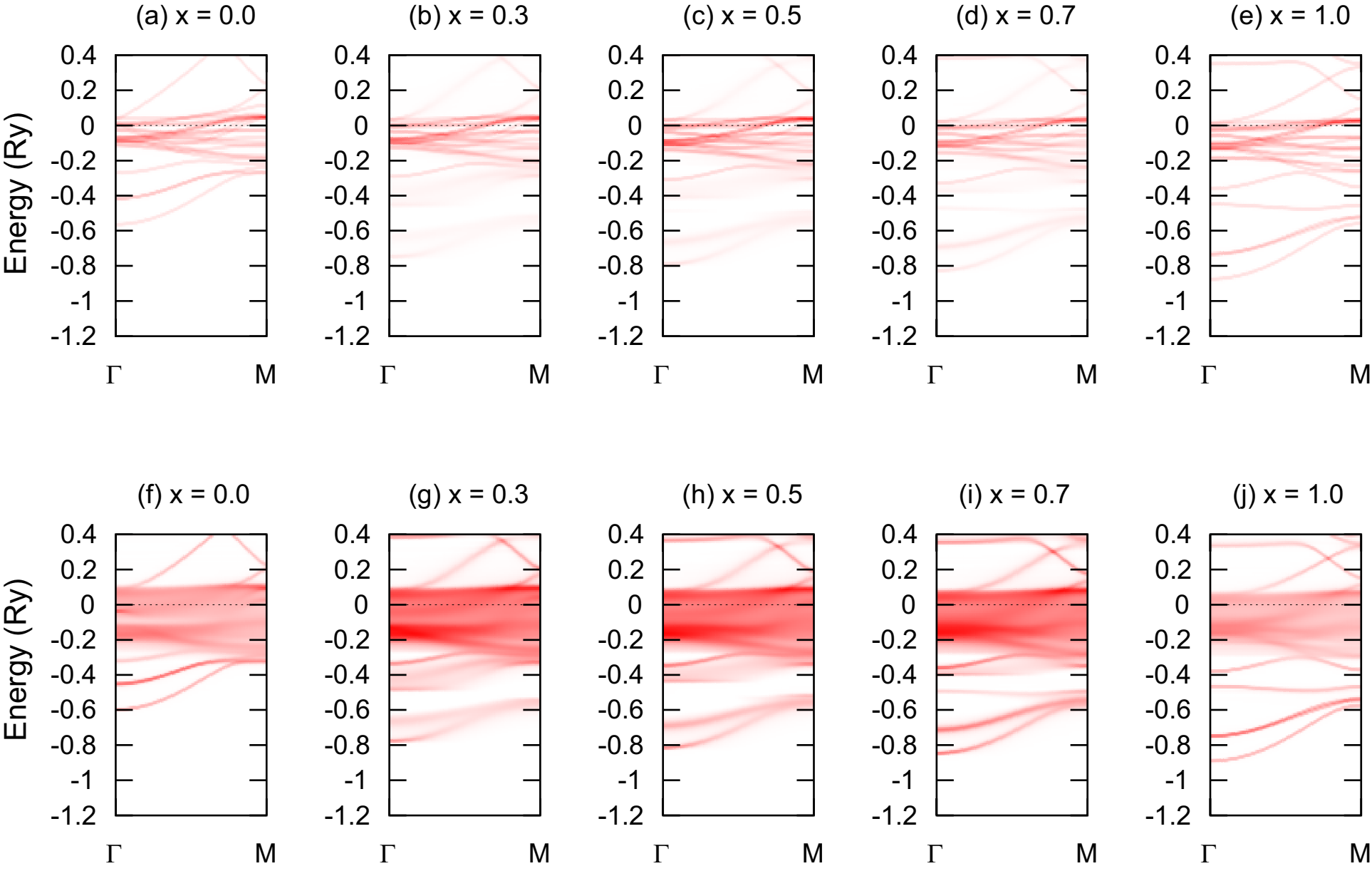
(a) x = 0.0
(b) x = 0.3
(c) x = 0.5
(d) x = 0.7
(e) x = 1.0
(f) x = 0.0
(g) x = 0.3
(h) x = 0.5
(i) x = 0.7
(j) x = 1.0
Energy (Ry)
0.4
0.2
0
-0.2
-0.4
-0.6
-0.8
-1
-1.2
Γ
M

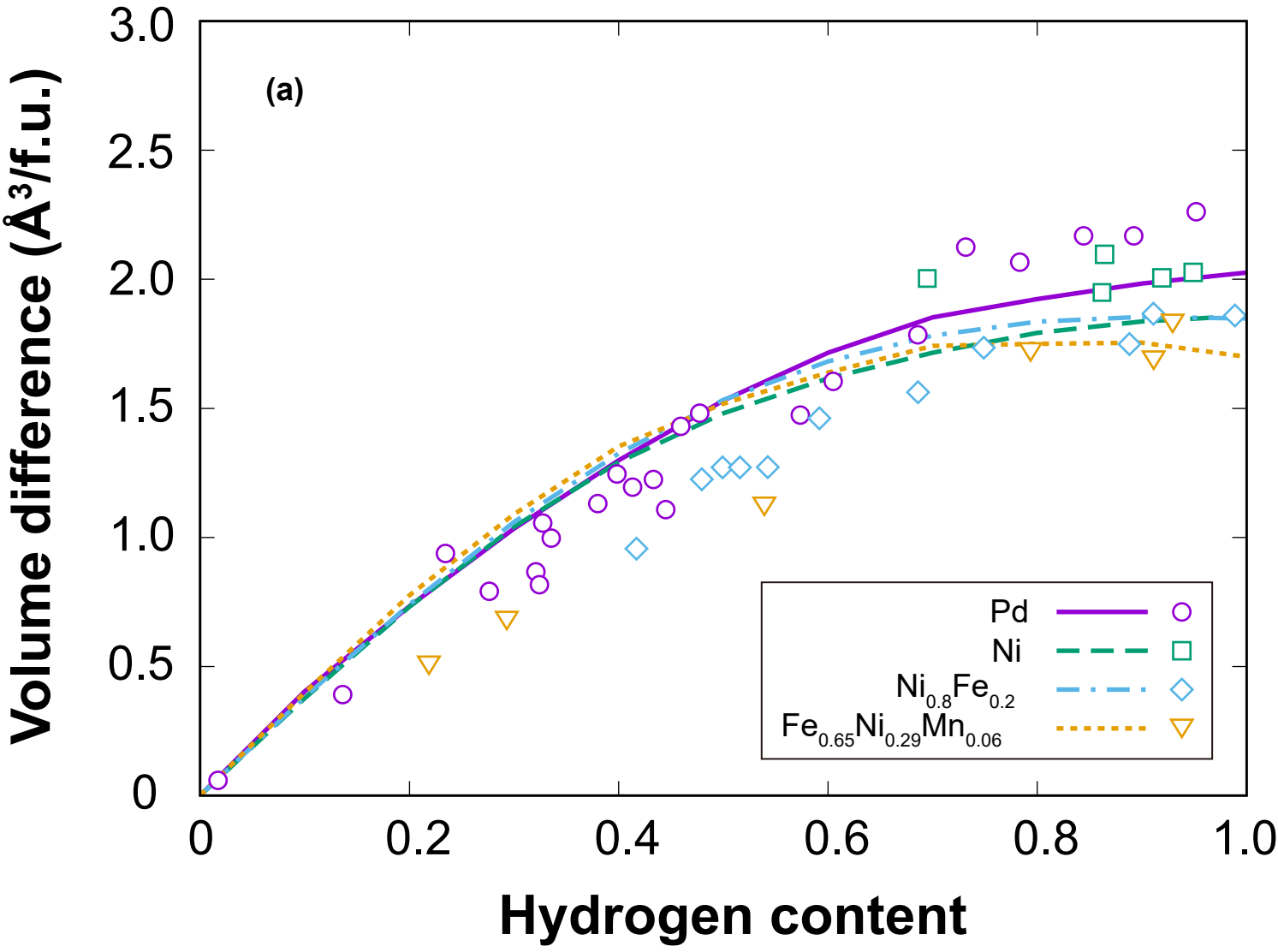
(a)
Volume difference (Å³/f.u.)
Hydrogen content
Pd
Ni
Ni0.8Fe0.2
Fe0.65Ni0.29Mn0.06

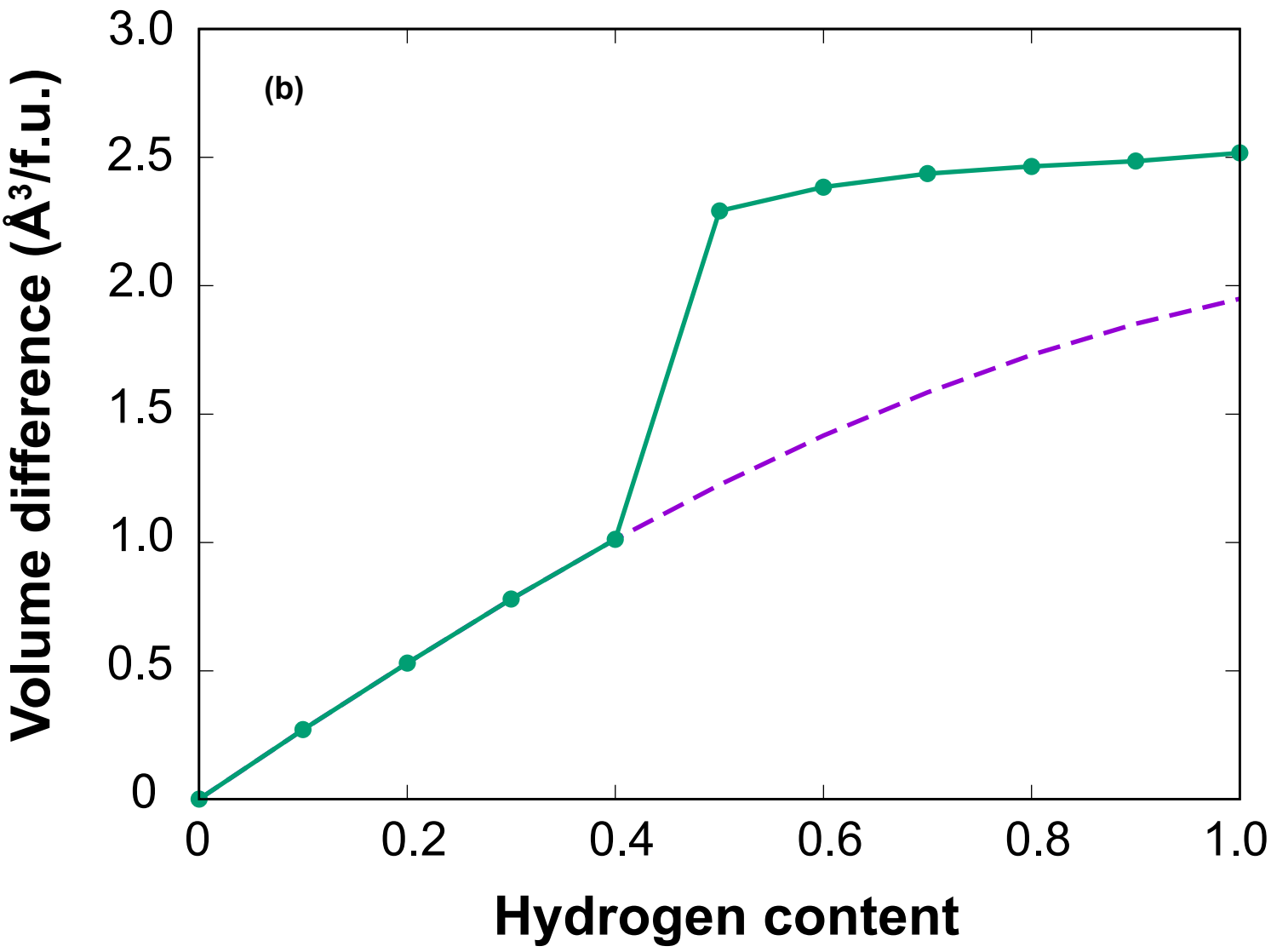
(b)
Volume difference (Å³/f.u.)
Hydrogen content

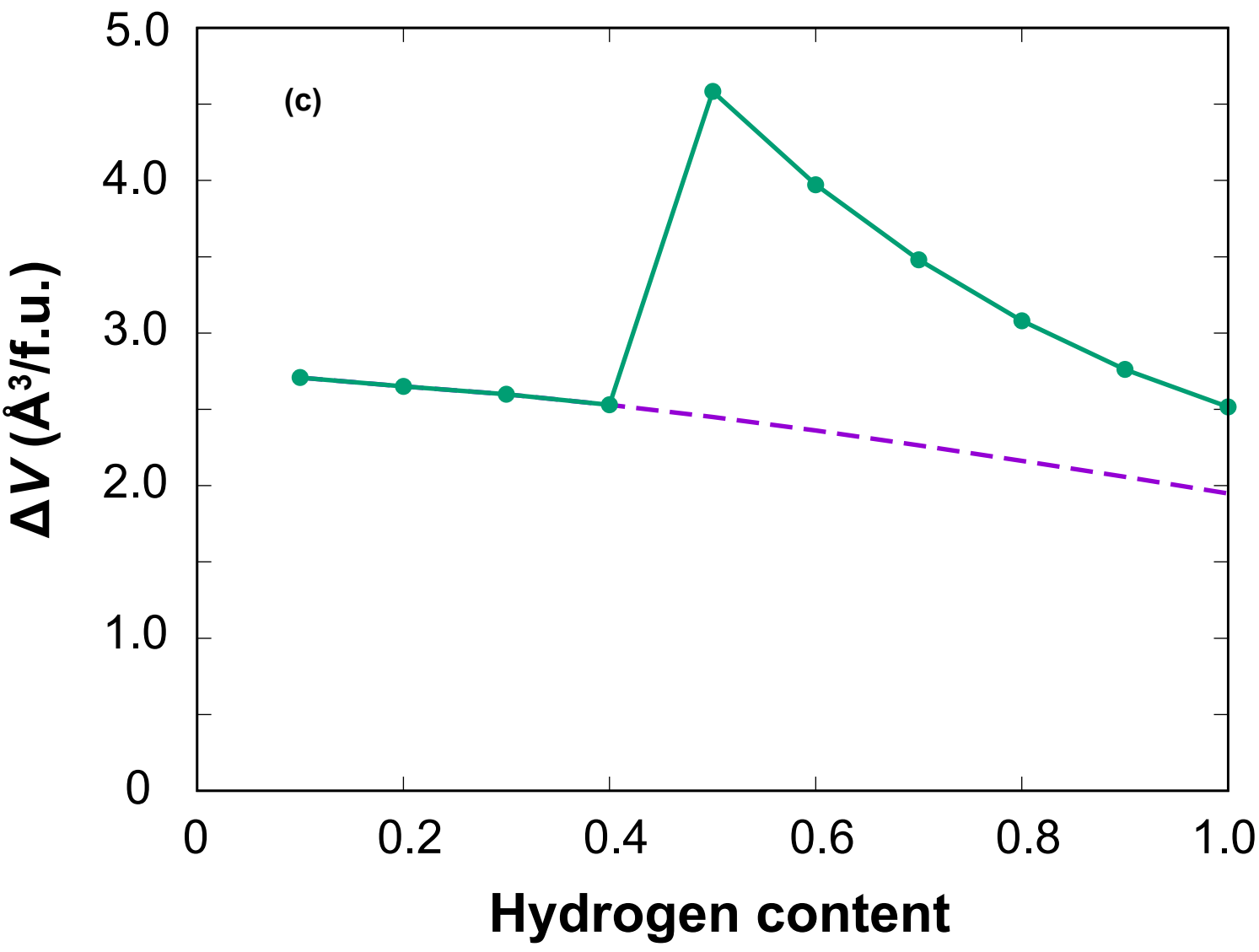
(c)
ΔV (Å³/f.u.)
Hydrogen content

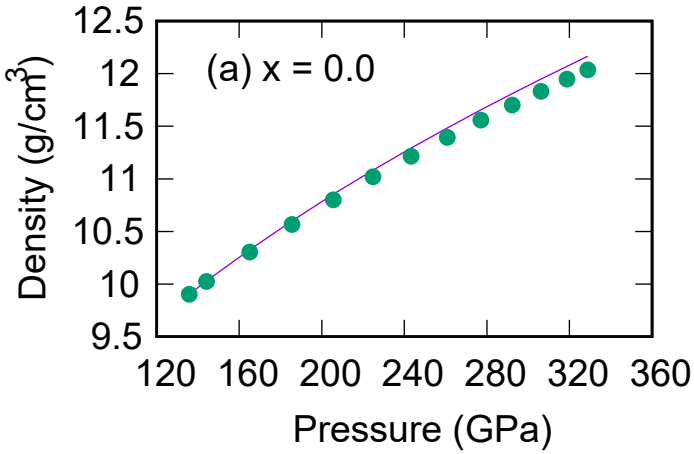
(a) x = 0.0
Density (g/cm3)
Pressure (GPa)
12.5
12
11.5
11
10.5
10
9.5
120 160 200 240 280 320 360

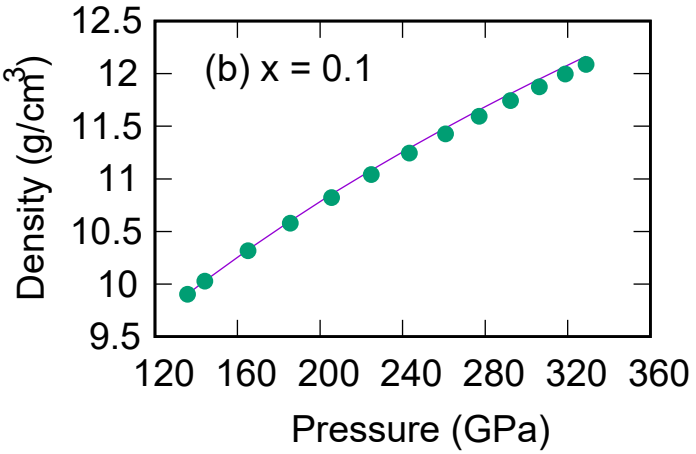
(b) x = 0.1
Density (g/cm3)
Pressure (GPa)
12.5
12
11.5
11
10.5
10
9.5
120 160 200 240 280 320 360

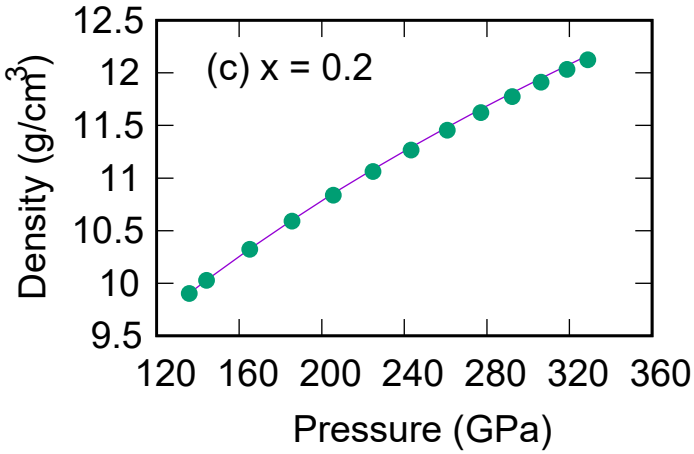
(c) x = 0.2
Density (g/cm3)
Pressure (GPa)
12.5
12
11.5
11
10.5
10
9.5
120 160 200 240 280 320 360

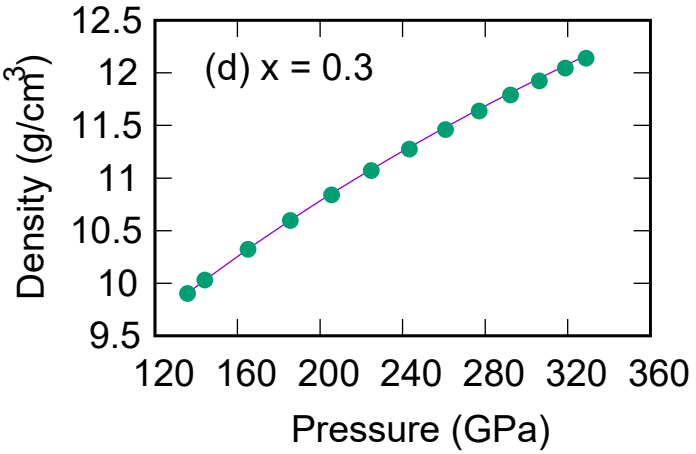
(d) x = 0.3
Density (g/cm3)
Pressure (GPa)
12.5
12
11.5
11
10.5
10
9.5
120 160 200 240 280 320 360

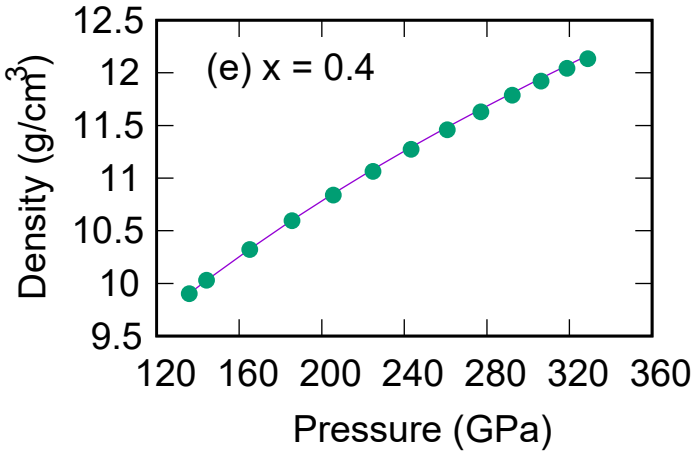
(e) x = 0.4
Density (g/cm3)
Pressure (GPa)
12.5
12
11.5
11
10.5
10
9.5
120 160 200 240 280 320 360

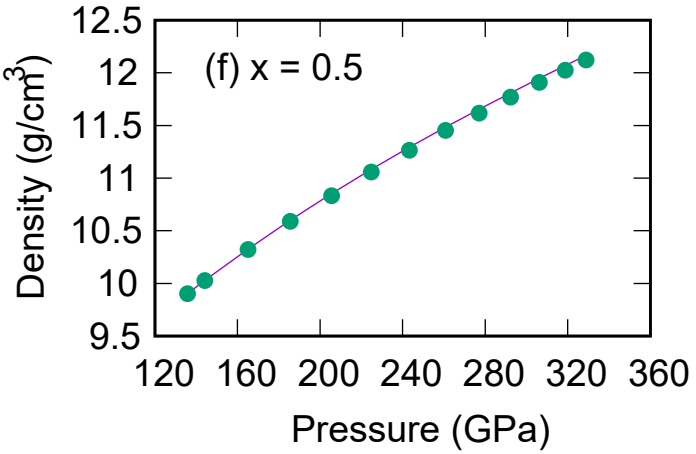
(f) x = 0.5
Density (g/cm3)
Pressure (GPa)
12.5
12
11.5
11
10.5
10
9.5
120 160 200 240 280 320 360

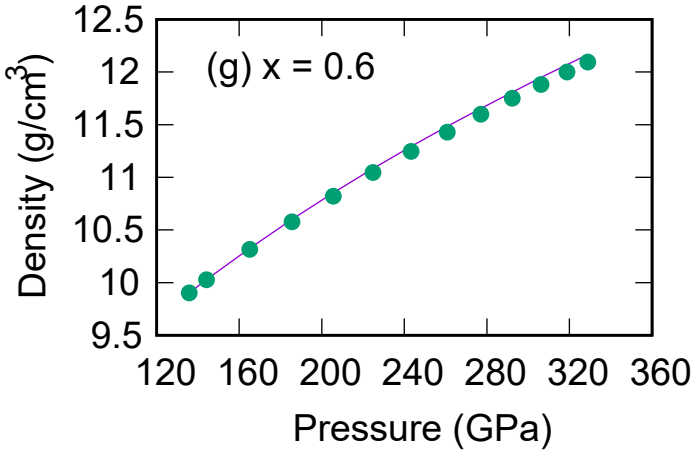
(g) x = 0.6
Density (g/cm3)
Pressure (GPa)
12.5
12
11.5
11
10.5
10
9.5
120 160 200 240 280 320 360

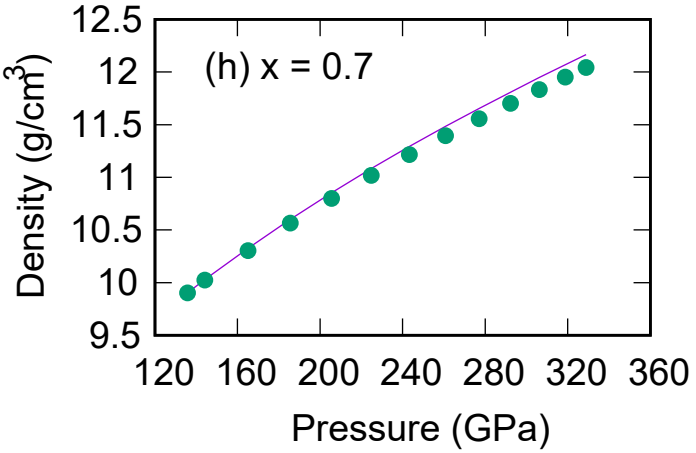
(h) x = 0.7
Density (g/cm3)
Pressure (GPa)
12.5
12
11.5
11
10.5
10
9.5
120 160 200 240 280 320 360

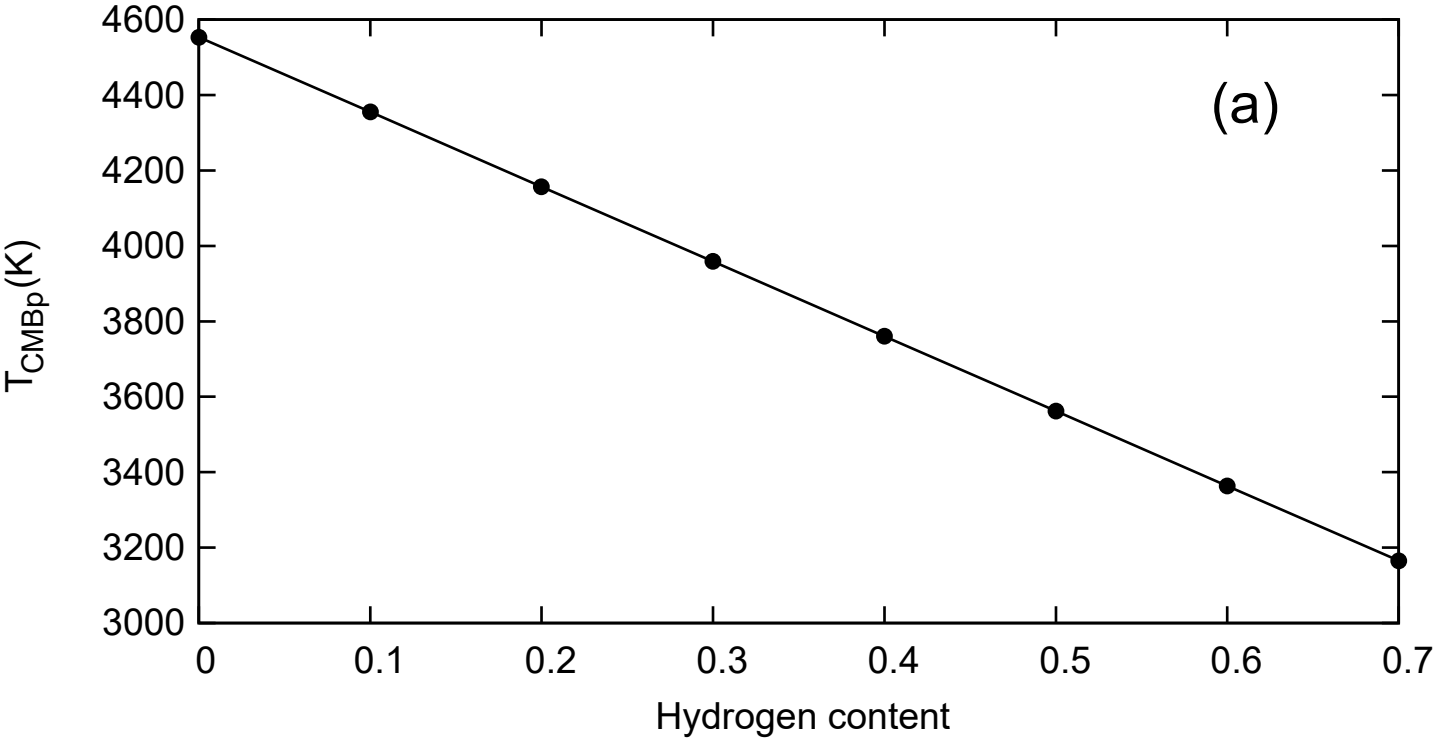
(a)
T_{CMBp}(K)
4600
4400
4200
4000
3800
3600
3400
3200
3000
0
0.1
0.2
0.3
0.4
0.5
0.6
0.7
Hydrogen content

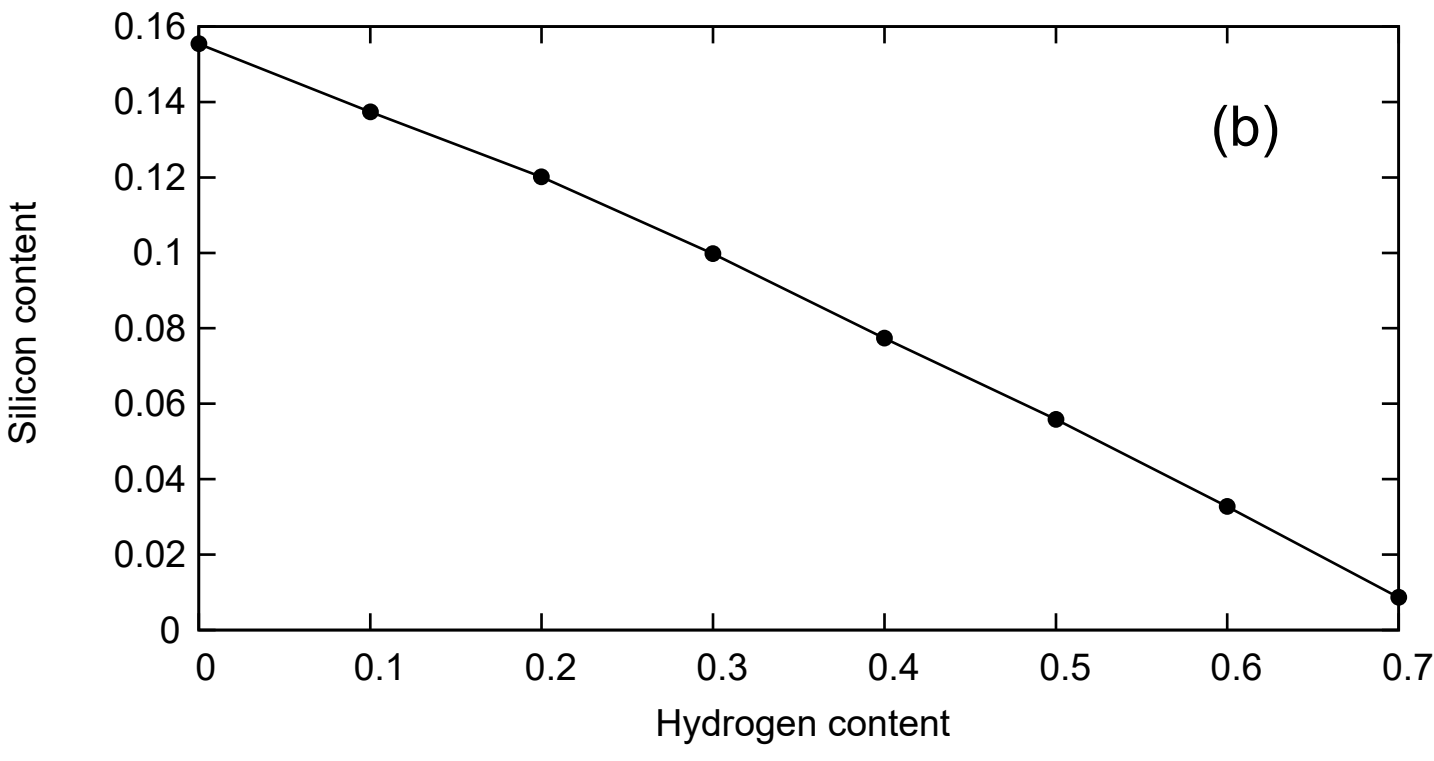
(b)
Silicon content
0.16
0.14
0.12
0.1
0.08
0.06
0.04
0.02
0
0
0.1
0.2
0.3
0.4
0.5
0.6
0.7
Hydrogen content

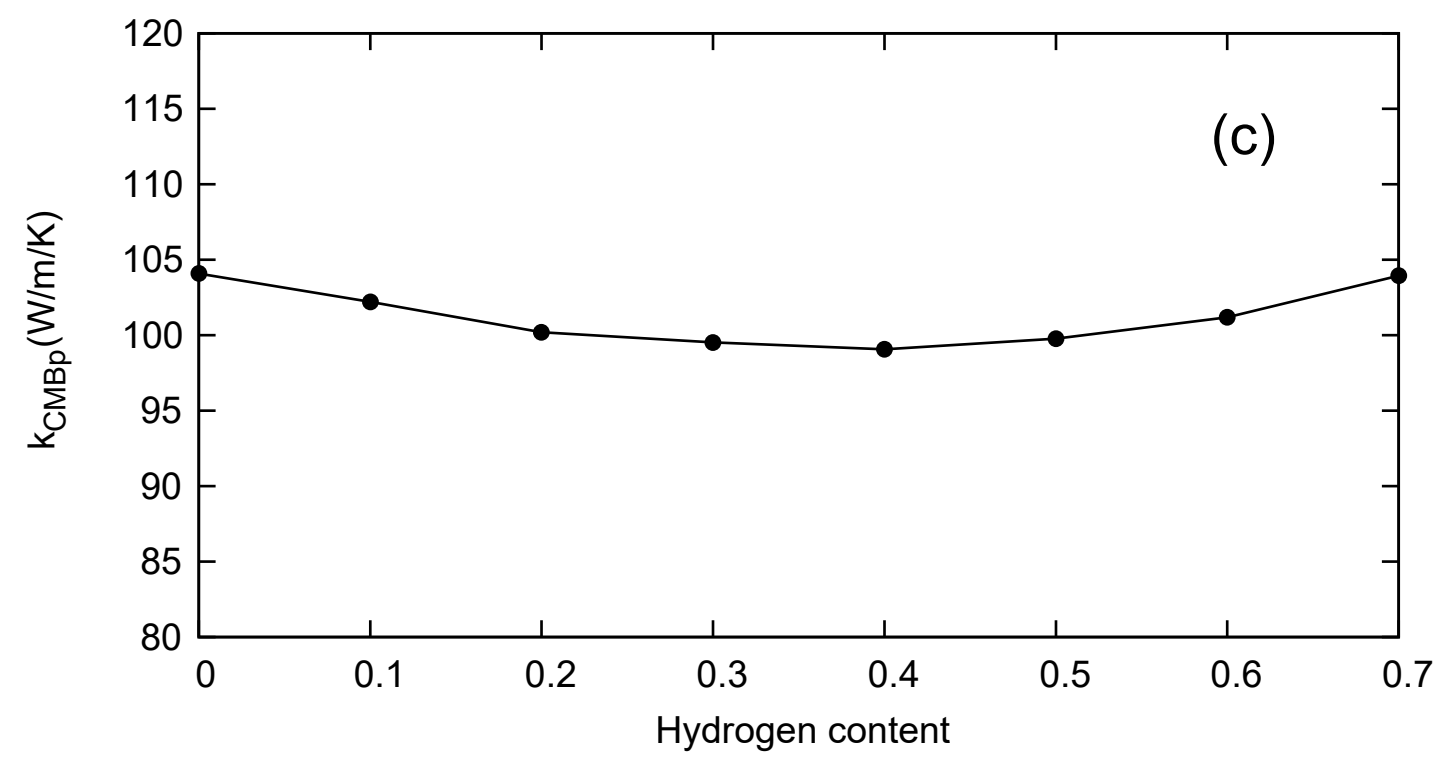
(c)
k_{CMBp}(W/m/K)
120
115
110
105
100
95
90
85
80
0
0.1
0.2
0.3
0.4
0.5
0.6
0.7
Hydrogen content

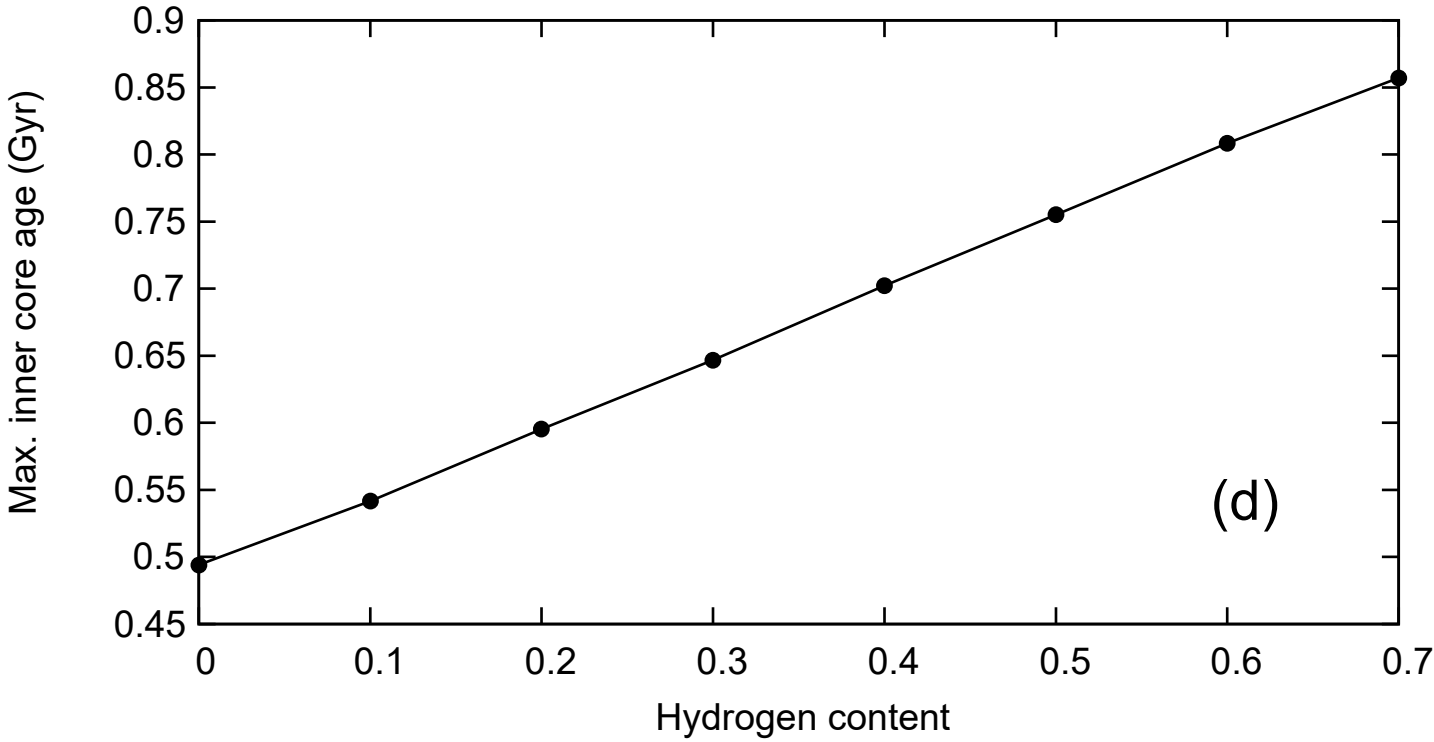
(d)
Max. inner core age (Gyr)
0.9
0.85
0.8
0.75
0.7
0.65
0.6
0.55
0.5
0.45
0
0.1
0.2
0.3
0.4
0.5
0.6
0.7
Hydrogen content